Cement and Concrete Research 210 (2026) 108384

Contents lists available at ScienceDirect

Cement and Concrete Research

journal homepage: www.elsevier.com/locate/cemconres

Modified bauxite residue blended cements – The effects of Na- and Al-rich pozzolans on phase assemblage and pore solution composition

Michael Wenzel [a,*], Fabien Georget [b], Thomas Matschei [c,a]

[a] Institute of Building Materials Research (ibac) RWTH Aachen University, Schinkelstraße 3, 52062, Aachen, Germany
[b] Department of Civil and Building Engineering, Université de Sherbrooke, QC, J1K 2R1, Sherbrooke, Canada
[c] iBMB Institute of Building Materials Concrete Construction and Fire Safety, TU Braunschweig, Beethovenstraße 52, 38106, Braunschweig, Germany

ARTICLE INFO

Keywords:
Hydration study
Activated bauxite residue
Blended cement
Alkali-effect
Aluminate rich pozzolans

ABSTRACT

Co-calcination, vitrification and reductive smelting transforms bauxite residues (BR) into reactive SCMs. This study investigates the impact of these treatments by comparing activated BR blended cements (10–50 wt% SCM) to: (1) evaluate SCM contribution to early hydration, (2) understand late-age microstructure, (3) detect internal durability issues and (4) identify promising binder concepts. Techniques like QXRD, isothermal calorimetry or ICP-OES were used to assess the systems early- and late-age properties. Our results link early-age properties to the mineralogy of the SCMs Na-bearing phases, while the pozzolanic reactivity correlates with bulk chemistry. 30 wt% Co-calcined/vitrified BR blends form a C-A-S-H dominated, aluminate hydrate-rich microstructure similar to LC^3 systems with Na and Fe enriched AFm and C-A-S-H phases. Hydrogarnet or strätlingite precipitation were observed in the most aluminate-rich blended systems. Ternary binders with 30 wt% co-calcined or 30–50 wt% vitrified BR were identified as promising low-clinker systems.

1. Introduction

The need to reduce the cement industry's carbon footprint is driving research. Low-clinker cements, based on Supplementary Cementitious Materials (SCMs), contribute to the industry's sustainability strategy [1,2].

After decades of application, fly ash (FA) and ground-granulated blast furnace slag (GGBFS) remain the benchmark (CEM II/B-V, CEM II/B-W or CEM III/A-C [3]) for new blended cements. The latter must achieve competitive durability performance [4,5], while remaining compatible with commercial admixtures and in-situ concrete production.

Increasing global SCM demand and decreasing supply of FA and GGBFS drive research on "alternative SCMs" [6,7]. To realize local, "Net-Zero" cements, the inclusion of high-volume waste streams (mining, metallurgy or combustion processes) is essential [7]. These materials show a wide range of mineralogies and contain various trace elements that may interfere with hydration reactions or environmental compatibility of blended cements. Quantitative knowledge of an SCMs impact on hydration kinetics and phase assemblage is necessary for optimizing blended cements, mitigating internal durability issues, and defining safe use-cases under field conditions.

Bauxite residue (BR) is a non-hazardous, metallurgical waste [8,9] abundant in countries such as Australia, China or Brazil (generation in 2020 ≈ 180 Gt/a [8]). It remains below the European thresholds for heavy metals and naturally occurring radioactive isotopes [8,10] in construction materials. While Cr and V are critical elements that, in some cases, surpass regulatory values [8], bauxite residues (BRs) usually meet national environmental compliance regulations for construction materials in Europe. They exhibit a complex mineralogy, with phases uncommon in cementitious systems. Understanding their impact on hydration is essential for optimizing blended cements and define possible use-cases.

Average BR produced via the Bayer process (primary alumina production) [11] shows the following oxide composition: CaO (6–10 wt%), SiO_2 (9–15 wt%), Al_2O_3 (15–20 wt%), Na_2O (3–9 wt%), TiO_2 (2–10 wt %) and Fe_2O_3 (30–50 wt%) [8]. The aluminate and silicate contents of BR make it a potential SCM, while its elevated Na_2O may pose a durability risk [12,13].

BRs' reactive components are either aluminates (mainly hydroxyoxides and hydroxides) or phases of the desilication product (DSP). The DSP, precipitated during the Bayer process [8,9,14], contains hydrates (Si/Al-hydrogarnet and N-A-S-H phases) and zeolitic Na-aluminosilicates. The formation of hydrogarnet and pozzolanic zeolite

* Corresponding author.
E-mail address: wenzel@ibac.rwth-aachen.de (M. Wenzel).

https://doi.org/10.1016/j.cemconres.2026.108384
Received 6 March 2026; Received in revised form 24 July 2026; Accepted 25 August 2026
Available online 8 September 2026
0008-8846/© 2026 The Authors. Published by Elsevier Ltd. This is an open access article under the CC BY license (http://creativecommons.org/licenses/by/4.0/).

phases (OH-sodalite/cancrinite) is competitive [15], causing variations in DSP composition and quantity.

Untreated BR is not reactive enough to be applied in binary blended cements with significant clinker and emission reductions, since 30 wt% substitution led to strength reductions of up to 40% [16]. Therefore, BR activation was investigated [8,18,19], and thermochemical treatments were developed to convert BR into a reactive SCM [19,20].

This study compares BRs activated via three processes: Co-calcination with kaolinitic clay (≈700 °C), vitrification (≈1250 °C) and reductive smelting (≈1600 °C) of Si- and Ca-enriched raw-materials. These processes [20–22] were developed within the Removal (EU Grant Agreement No. 776469) and ReActiv (EU Grant Agreement No. 958208) projects. The R^3 reactivities of modified BRs range between 250 and 800 J/g_{SCM} [8]. Previous studies [19,20] already demonstrated reactivity and strength potential of co-calcined and vitrified BR-blended cements. Building on these findings, this work investigates modified BR-blended cements in a wider compositional range (10 to 50 wt% SCM and ternary BR/limestone blends).

Co-calcined BRs retain some oxidic and zeolitic phases of untreated BR [20], while vitrification and reductive smelting completely transform the mineralogy. The activation treatments energy consumption differs and yields SCMs of distinct phase assemblages that affect silicate, aluminate and calcium availabilities. The objective of this study is to quantify these effects, by investigating the microstructure and pore solution compositions of these SCMs in comparable binder designs. We aim to understand how the choice of activation affects hydrate nucleation and pozzolanic regime of modified BR, governing the phase assemblage evolution of the blended cements.

A special emphasis is placed on the role of modified BRs in the alkali acceleration of hydration and pozzolanic reactions, since the activation treatments change the SCMs Na-bearing phases. Previous studies [19,20] implied that changes in Na-release might explain the significant strength differences between co-calcined and vitrified BR blended systems during the first days. This study provides novel insights into how Na release rates drive the early-hydration of modified BR containing cements. It assesses how Na release from zeolitic and glassy Na-bearing phases affects pore solution composition and phase assemblage evolution.

The works main novelty is a consistent microstructural dataset, covering modified BR-blended cements between 1 and 180 days. This is achieved by combining experimental techniques that link SCM properties (physical, chemical and mineralogical) with hydration behavior, the results of reactivity tests (R^3 test [23], SLiM test [24]), and engineering properties.

Finally, this work links late-age morphology, phase assemblage and pore solution composition via thermodynamic modeling. OPC and fly ash (FA) blended cements were included to provide a microstructural baseline for the discussion. A complete list of abbreviations is provided in Appendix A.

2. Materials and methods

2.1. Scientific approach

Fig. 1 illustrates the studies methodological framework across the hydration timeline. To understand the impact of SCMs on hydration, their physical properties (PSD, SSA, density), elemental composition (XRF), phase assemblage (QXRD, TGA) and amorphous phases (Raman/FTIR spectroscopy) are characterized. The SCMs' early-age reactivity was evaluated (SLiM test) and linked to paste-scale results (calorimetry, Mini-Cone Test). Quantitative phase assemblages of hydrating paste (1 to 180 d) were determined using QXRD and TGA, while mature pastes were further analyzed with SEM-EDX, ICP-OES and ion-chromatography. The 180 d compressive strength was used to link microstructural data with macroscopic performance. The dark blue arrows in Fig. 1 indicate the sequence, in which analytical methods are introduced in the Methods section, corresponding to their application along the hydration timeline.

2.2. Methods

2.2.1. Characterization of raw materials

Particle size distribution (PSD), specific surface area (SSA) and true density of the anhydrous binder components were determined using lasergranulometry, N_2-adsorption and He-pycnometry, respectively. The SSA was determined on dried samples (2–3 g) using a 3P

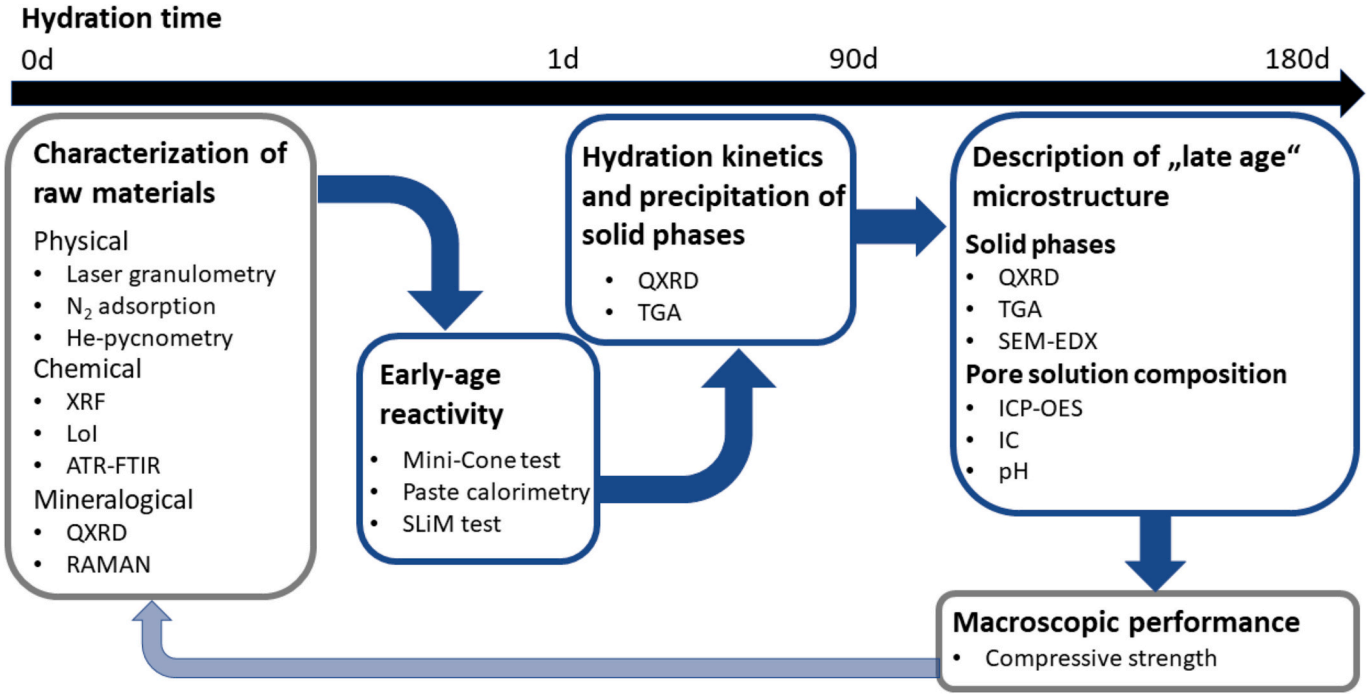


Fig. 1. Summary of the analytical methods and their contributions to this study. The full names of the analytical methods are included in Appendix A (Table A6).

Instruments Sync 220A physisorption analyser and calculated using the Brunauer-Emmett-Teller isotherm. The PSD was determined on samples dispersed in isopropanol using a Better Sizer 3S plus laser-diffractometer and the Mie scattering model. True density was determined at 25 °C by He pycnometry using 2–3 g of dried sample with an Accupyc III 1250. For all methods, three independent measurements were averaged for each material.

To obtain the raw materials element composition loss on ignition (LoI) and X-ray fluorescence spectroscopy (XRF) experiments were conducted. LoI was determined according to EN 196-2 using 1.00 ± 0.05 g of sample and a peak-temperature of 950 ± 25 °C. For XRF analysis, 1.4 g of sample (ground <125 μm) were mixed with $Li_2B_4O_7$ and LiBr at a 1:9 ratio, fused (Malvern PANalytical LeNeo fluxer, 1050 °C) into glass beads and measured using a Bruker S8 Tiger Series 2 spectrometer.

The mineralogy of the binder components was assessed through X-ray diffraction (QXRD) and subsequent Rietveld refinement. Ground samples (<63 μm) were backloaded and analyzed using a PANalytical X'Pert Pro diffractometer (Cu Kα radiation, 40 kV, 40 mA, Bragg-Brentano geometry) equipped with an X'Celerator detector. The optical configuration included a 240 mm goniometer radius, 0.04 rad soller slits, 10 mm incident beam mask, 0.125° divergence slit, Ni filter and 5° anti-scatter slit. A spinning stage and a beam knife were used to reduce preferred orientation and low angle scattering. Scans were performed from 6.000 to 54.964° 2θ, with a step size of 0.0334° (scan time ≈ 45 min). Rutile (Kronos, 94.14 wt% crystallinity) was used as an external standard. Spectroscopic methods were employed to characterize the X-ray-amorphous of the modified BRs. Dried (110 °C) and ground (<63 μm) SCM was used to collect FTIR spectra (450 to 4000 cm^{-1}, resolution 4 cm^{-1}) using a Perkin Elmer Spectrum 2 (ATR mode). To obtain Raman spectra, dried samples (110 °C) were mixed with epoxy resin (Struers, EpoFix) and cast into 25 mm cylindrical molds. The cured specimens were polished with 1 μm diamond suspension using a Buehler Automet 300. The spectra (0–4000 cm^{-1}) were collected using a WITec alpha 300R Raman microscope equipped with a 532 nm Nd:YAG laser coupled with a RayShield.

To quantify the SCMs' reactivity the R^3 data published in [8] are reused. The SCMs early-age reactivity was assessed using the sulfate-limited-model-system (SLiM) developed by Muzenda and Demeusy [24,25]. The SLiM paste consists of SCM (74.1 wt%), $Ca(OH)_2$ (18.5 wt %), and $CaSO_4{\cdot}2H_2O$ (7.4 wt%) (all chemicals VWR, purity >98 wt%). Pastes of w/s = 1.0 were mixed for 2 min at 1600 rpm (IKA Eurostar 60 Digital). Samples (15.000 ± 0.100 g) were filled into 25 mL ampoules and measured in a Calmetrix I-Cal Ultra calorimeter at 20 °C (72 h, logging frequency = 0.017 Hz). Results represent the average of two replicates per SCM.

2.2.2. Fresh samples and calorimetric measurements

To assess the effect of SCM content on structural build-up, the flow spread of three independent batches per composition was measured 0, 10, 20 and 30 min after mixing. Slump loss (Δs) was calculated using Eq. (1).

$$\Delta s = \left(1 - \left[s(0)/s(30\ \text{min})\right]\right)*100 \quad (1)$$

With: s(t) = mini cone slump as function of time and Δs = slump loss [mm].

Isothermal calorimetry was used to measure the heat flow of cement pastes, which were prepared following the mixing regime of Section 2.5. Samples (15.000 ± 0.100 g) were placed in 25 mL ampoules and measured for 72 h at 20 °C using a Calmetrix I-Cal Ultra calorimeter. Results represent the average of two replicates per binder.

2.2.3. Analysis of hydrated samples

The phase assemblages of hydrated samples were quantified on paste (Two 3–5 mm thick discs cut from water-saturated paste, wet-ground with P1200 SiC paper and measured). A PANalytical X'Pert Pro diffractometer with the optical setup reported in Section 2.2.1. was utilized. The step time was reduced to reach a shorter scan time and minimize carbonation/drying related artefacts (≈27 min), otherwise the same settings were used. Rutile (Kronos, 94.14 wt% crystallinity) served as external standard. The analysis was performed using PANalytical HiScorePlus (v5.1) software. Custom mass absorption coefficients were calculated [26] and the ICSD codes of the refined phases are provided in the supplementary information.

Based on the Rietveld results normalized portlandite (R_{CH}) contents were calculated using Eq. (2) to compare pozzolanic reactivity.

$$R_{CH}(t) = b(t)_{CH\ blended}/CF*b(t)_{CH\ OPC} \quad (2)$$

With: $R_{CH}(t)$ = normalized CH content, b(t) CH blended = Portlandite content in blended cements [$g/100g_{paste}$], CF = clinker factor of the blended cement [−] and $b(t)_{CH}$ OPC = Portlandite content in OPC reference [$g/100g_{paste}$].

Thermogravimetric analysis of 28 or 180 d hydrated cement pastes verified the Rietveld results (see Fig. S 10) and determined total bound water contents. TGA measurements were performed on 30–50 mg of ground, solvent-exchanged samples using Al_2O_3 crucibles and a Mettler Toledo STARe 1 TGA/DSC. After 10 min of isothermal hold (30 °C) the samples were heated (10 K/min) to 1050 °C under a N_2 flow of 100 mL/min. Portlandite and $CaCO_3$ amounts were calculated from TG weight loss using the tangential method [27]. The temperature ranges for phase decomposition were determined using the first derivative of the thermogravimetric curve (CH ≈ 420–440 °C, $CaCO_3$ ≈ 600–800 °C). A stoichiometric release of 1 mol H_2O per mole CH and 1 mol CO_2 per mole $CaCO_3$ were assumed.

To obtain an additional indication of the systems' water uptake a semi-quantitative water balance was attempted for 180 d cured pastes. Total bound water was defined as the TGA mass loss between 50 and 550 °C. The free water was estimated by subtracting the total bound water from the mixing water.

The water bound in the X-ray amorphous was approximated by subtracting, the water released from portlandite (ICSD 202220) and aluminate hydrates (assumed AFt = ICSD 155395, monosulfate = ICSD 100138 and monocarbonate = ICSD 59327) from the total bound water. The water released from CH was taken from the TGA signal, while the amounts released by AFt and AFm were calculated based on the QXRD results. The water contents of the present AFm phases may differ from the assumed ones [28] and introduce an unknown error.

SEM-EDX was used to visualize the morphology of the hydrated pastes and analyse the composition of C-A-S-H and AFm phases. The samples were vacuum-impregnated with epoxy resin and polished using 1 μm diamond suspension (Buehler, Automet 300). A 5 nm tungsten coating was applied (Leica ACE600 coater). SEM-EDX mapping was performed using a Zeiss Supra S55 SEM equipped with in-lens BSE detector and an Oxford instruments X max 150 EDX detector (working distance = 8.5 mm, acceleration voltage = 15.00 kV, sample current ≈ 2 nA). EDX hypermaps (≈ 222 × 271 μm maps, after standardless quantification using Aztec software) were acquired. They were processed with the Python-based GLUE interface [29,30] using EDXIA plugins [31].

2.2.4. Analysis of pore solution

450 g of binder were mixed with 225 g of deionized water following the mixing regime of EN 196-1. The w/b ratio was chosen to extract 2 to 5 mL of solution during one experiment. The paste was poured into 250 mL PE bottles, which were sealed with silicone (DOWSIL 732®) and stored for 90 d at 20 °C. The pore solution was extracted (maximum pressure 200 MPa) and collected in argon-filled HDPE bottles. The solution's pH was measured immediately (Mettler Toledo, Inlab Expert NTC 30 electrode, calibrated with 0.003 to 1 mol/L NaOH solutions).

Extracts were diluted 1:200 (deionized H_2O, conductivity <0.055 μS/cm) and acidified to pH 2 using 1% HNO_3 (Merck, Supelco®, for trace analysis) for ICP-OES measurements. To quantify SO_4^{2-}, Cl^- and NO_3^-, 1 mL of pore solution was diluted with deionized water (1:50). All samples were stored at 5 °C and analyzed within 14 days.

The main elements were quantified using an Agilent Technologies 5100 ICP-OES, equipped with quartz-glass torch, glass double pass spray chamber and OneNeb series 2 nebulizer. Multi-element standards were prepared from single-element reference solutions (PerkinElmer, 10,000 mg/L). A given wavelength was used for quantification if (1) the calibration curve R^2 value exceeded 0.98 and (2) a defined emission band was present in sample and standard. SO_4^{2-}, Cl^- and NO_3^- were quantified by ion chromatography (Metrohm ECO IC) using a Metrosep A Supp 19–150/2.0 column, isocratic elution (8.0 mmol/L Na_2CO_3 + 0.25 mmol/L $NaHCO_3$) and external calibration standards (0.1–10 mg/L of Na_2SO_4, $NaNO_3$, and NaCl). Samples (10 μL) were manually injected. The results from IC and ICP OES are reported as the average of duplicates.

Saturation indices (SI) were calculated at 20 °C, standard pressure, and oxidizing conditions using the GEM-Selector software. The PsiNagra [32] (ionic-species and common minerals), CEMDATA18 [33] (clinker phases and cement hydrates), Claysore [34] (clay minerals), and Zeolite23 [35–37] (OH-sodalite and selected zeolites) thermodynamic databases were used. Activity coefficients were derived via modified Debye-Hückel theory (Helgeson) [38]. CEMDATA18's CSH II model was used, including only jennite and tobermorite endmembers, while ignoring alkali-sorption in C-A-S-H. Solid-phase precipitation was manually suppressed.

2.2.5. Mortar samples and compressive strength

Mortars (w/b = 0.5) were prepared according to EN 196-1. The flow spread was adjusted to 200 ± 10 mm using Master Glenium ACE 460. After demolding (24 ± 1 h), the specimens were water-cured for 179 d. Compressive strength was measured using a Norm test 2060 universal testing machine (Toni Technik Baustoffprüfsysteme GmbH). The strength activity indices (SAIs) were calculated according to Eq. (3). The error bar equals the sum of the relative errors of the used strength values.

$$SAI(t_i) = \frac{\sigma_{blended\ cement}(t_i)}{\sigma_{OPC}(t_i)} \quad (3)$$

With: SAI (t_i) = strength activity index [−], $\sigma_{blended\ cement}(t_i)$= Compressive strength of the blended cement [MPa], $\sigma_{OPC}(t)$ = compressive strength of the OPC reference [MPa] and t_i = hydration time [d].

2.3. Characterization of raw materials

This study compares BR-based SCMs developed within the ReActiv project. They were produced and supplied by consortium members. Activation processes and initial performance data of the BR-based SCMs are reported in [20,21,39]. Three co-calcined BRs (COCA, COCB, COCC), based on the residues of different alumina plants, one vitrified BR (VBR) and one reductively smelted BR (SL) were investigated using untreated BR and siliceous fly ash (FA) as references. All binders used the same OPC (CEM I 52.5 N, HOLCIM Saint Pierre La Cour plant). Commercial limestone powder (Omyacarb AL 5) was used in selected binders.

The untreated BR was dried to constant mass at 50 °C (Nabertherm N7H).

Following the protocol of Peys et al. [20], the different BRs were interground with 20 wt% (COCA/COCB) and 10 wt% (COCC) of pure kaolinite and co-calcined in a muffle furnace at 750 °C and oxidizing conditions. The co-calcined BRs span the range of reactive DSP compositions commonly observed in Bayer residues [8]. The lower kaolinite addition in COCC compensated for its higher reactive DSP content, resulting in a R^3 reactivity comparable to COCA and COCB [8]. For homogenization BR, COCA, COCB and COCC samples were ball-milled for 45 min (Welte Mahltechnik GmbH).

For vitrification, BR was interground with SiO_2, CaO (fluxes), and carbon to achieve partial melting and reducing conditions using a TF 4000 induction furnace [19]. The raw meal composition was thermodynamically optimized by Hertel et al. to minimize melting temperature (1250 °C) and convert Fe-bearing phases into magnetite before water quenching and grinding, as reported in [21].

The smelted BR slag (SL) was produced by Sparis et al. [22]. BR was fluxed with CaO, $NaClO_3$ and ilmenite ($FeTiO_3$) to produce a ferrotitanium alloy and reactive slag in an aluminothermic process. After smelting in an Ar-filled induction furnace (1500 ± 50 °C), the melt was air-quenched, materials mechanically separated and ground.

Table 1 presents the bulk oxide composition of the anhydrous raw materials as determined by XRF. The materials are compared property-by-property. VBR has the lowest Al_2O_3 content (18.7 wt%), followed by BR, COCA-COCC (24–30 wt%) and SL (52.4 wt%). The alumina levels of VBR and co-calcined BRs (COCBRs) are comparable to fly ash (FA).

The SiO_2 + CaO content of VBR (35.3 wt%, Si/Ca = 1.0) falls between SL (42.2 wt%, Ca/Si ratio = 1.2) and COCBRs (20 to 30 wt%, Ca/Si ratio < 0.5), all of which are lower than the reference FA (57.4 wt%, Ca/Si = 0.06). The Si/Al ratios of BR-based SCMs range from 0.40 (BR) to 0.96 (VBR), highlighting their aluminate-rich nature (FA: Si/Al = 2.13). Among the COCBRs, the Si/Al ratio increases from 0.58 (COCA) to 0.76 (COCC).

Due to high Fe contents, the densities of BR-based SCMs (3.2–3.4 g/cm^3) surpass those of OPC (3.1 g/cm^3) or FA (2.2 g/cm^3), as shown in Table 1. The particle size distributions (PSDs) of the activated BRs are comparable to OPC (CEM I 52.5 R). The specific surface area (SSA) does not correlate with the median particle sizes (D_{50}). VBR and SL have SSAs similar to OPC (0.8–2.0 m^2/g), while BR, COCA, COCB and COCC exhibit SSAs between 10 and 20 m^2/g. The inconsistency of modified BRs' PSD and SSA results from the agglomeration of nm-sized particles in BR and COCBRs. As discussed in [8,20,40], the SSA differences of the modified BRs influence workability and structural build-up of blended cements.

The mineralogy of modified BR is defined by the activation treatment. Table 2 summarizes the results of the XRD Rietveld refinement, categorizing the phases as: (1) residual phases from bauxite ore, (2) DSP phases, (3) minerals formed during thermochemical activation treatments, and (4) clinker phases and Ca-sulfates. Inert crystalline phases are assigned to subgroups 1 or 3. Co-calcination reduces the amounts of inert minerals inherent to BR (subgroup 1) and triggers hematite formation (subgroup 3). Hematite was identified via XRD and shows notable peak-broadening. The reactive phases in co-calcined BRs are metakaolin and partially dehydroxylated zeolitic phases of the DSP (subgroup 2).

During the transformation of BR into COCB, a partial decomposition of cancrinite occurred. Cancrinite content decreased from 12.9 (BR) to 5.7 wt% (COCB). About 2 wt% of cancrinite loss are attributed to kaolinite addition to the mix, suggesting the formation of X-ray-amorphous phases, during co-calcination, with an estimated degree of amorphization of ≈56%. A shift of the d_{110} spacing (6.325 to 6.006 Å) also suggests changes in the zeolitic cage structure as visualized in Fig. S 8. If figures or tables are referenced with an A before the number they are included in the appendix, if they are highlighted with an S, they are included in the supplementary files. While this warrants further investigation, our observation could explain the synergistic reactivity increase reported for COCBRs [20]. BR and COCBRs retain traces of clay minerals.

VBR contains spinel's of the magnetite-hercynite solid solution as the main iron bearing phase. According to Giels et al. ulvöspinel, titanomagnesite and nanocrystalline wüstite (dendrites originating from larger magnetite-hercynite SS crystallites) are also present [41]. Iron-rich dendrites, attached to larger spinels, were confirmed via SEM-

Table 1
Bulk oxide composition and physical characteristics of anhydrous raw materials. The element composition of COCA, COCC and COCB are courtesy of A. Peys [20], the composition of VBR is courtesy of T. Hertel [21].

Oxides [wt% anhydrous]	BR	COCA	COCB	COCC	VBR	SL	FA	OPC	LS
Fe_2O_3	39.6	45.0	35.6	38.3	34.7	1.9	5.8	3.0	0.1
Al_2O_3	21.5	23.9	30.4	25.6	18.7	52.4	25.8	5.0	0.1
K_2O	0.3	0.3	0.3	0.2	0.1	0.0	0.2	0.9	–
SiO_2	8.7	18.1	17.8	20.7	18.0	19.6	54.3	20.7	0.3
Na_2O	4.3	4.6	3.4	9.1	7.0	0.4	0.4	0.3	–
CaO	8.0	3.6	7.4	1.2	17.5	22.6	3.6	65.3	55.5
TiO_2	3.7	4.1	4.8	4.6	2.8	1.4	1.3	0.2	–
SO_3	–	0.1	0.1	0.1	0.1	0.1	0.2	3.2	–
V_2O_5	–	0.1	0.1	0.1	0.2	<0.1	0.0	0.0	–
Cr_2O_3	0.1	0.1	0.1	0.1	0.3	0.0	0.1	0.1	–
Mn_2O_3	<0.1	<0.1	<0.1	<0.1	<0.1	<0.1	0.1	0.1	–
P_2O_5	–	–	–	–	0.2	<0.1	0.7	0.2	–
ZrO_2	–	–	–	–	–	–	0.1	0.1	–
SrO	–	–	–	–	–	–	0.2	0.1	–
MgO	–	–	–	–	–	0.6	1.4	–	–
LoI	9.3	<0.1	<0.1	<0.1	0.4	0.0	5.8	0.9	44.0
Sum	100.0	100.0	100.0	100.0	100.0	100.0	100.0	100.0	100.0
True density [g/cm^3]	3.42	3.43	3.28	3.32	3.40	3.02	2.25	3.13	2.76
$D_{10}/D_{50}/D_{90}$ [µm]	0.5/2.7/38	1.7/6.1/41	1.7/5.1/32	1.8/5.9/30	3.7/9.5/32	2.6/12.6/38	4.2/21.1/81	2.3/13//37	1.8/5.1/16
Specific surface area BET [m^2/g]	10.81	19.75	12.70	12.57	0.81	1.20	4.65	1.26	1.65

Table 2
Mineralogical composition of anhydrous raw materials. A detection limit of 0.5 wt% was assumed for all phases and the ICSD files used for the refinements are tabulated in the supplementary materials.

Mineral phases [wt% anhydrous]	BR	COCA	COCB	COCC	VBR	SL	FA	OPC	LS
1 - Residual phases from bauxite parent ore									
Goethite	5.4	–	–	0,7	–	–	–	–	–
Hematite*	32.4	30.9	24.3	22.2	–	–	0.6	–	–
Gibbsite	3.2	–	–	–	–	–	–	–	–
Bayerite	1.0	–	–	–	–	–	–	–	–
Boehmite	1.6	–	–	–	–	–	–	–	–
Diaspore	11.5	–	–	–	–	–	–	–	–
Corundum	–	–	5.5	0	–	–	–	–	–
Quartz	0.5	0.8	1	2.2	–	–	8.6	–	–
Anatase	0.4	0.1	0.3	1.5	–	–	–	–	–
Rutile	–	1.2	–	0.4	–	–	–	–	–
Zircon	1.5	–	–	0.1	–	–	–	–	–
Perovskite	–	–	0.8	–	–	–	–	–	–
Ilmenite	–	–	–	–	–	–	–	–	–
Brookite	0	–	–	–	–	–	–	–	–
Calcite	4.7	–	–	–	–	–	0.4	–	100.0
Muscovite/Illite	2.5	1.6	–	0.1	–	–	–	–	–
Kaolinite	–	–	0.6	–	–	–	–	–	–
2 - DSP phases									
Sodalite	–	3.5	–	9.9	–	–	–	–	–
Cancrinite	12.9	–	5.7	–	–	–	–	–	–
Hydrogarnet	–	–	3.5	–	–	–	–	–	–
Grossular	–	1.9	0.7	–	–	–	–	–	–
3 - Crystalline phases formed via thermochemical activation									
Albite	–	–	–	0.6	–	–	–	–	–
Nepheline	–	–	–	–	–	–	–	–	–
Mullite	–	–	–	–	–	–	16.4	–	–
Hibonite	–	–	–	–	–	11.5	–	–	–
magnetite	–	–	–	–	29.2	–	–	–	–
4 - clinker phases and Ca-sulfates									
C_3S (M3)	–	–	–	–	–	–	–	66.8	–
C_2S (ß)	–	–	–	–	–	–	–	12.6	–
C_4AF	–	–	–	–	–	–	–	8.2	–
C_3A (cub.)	–	–	–	–	–	–	–	5.2	–
C_3A (ort.)	–	–	–	–	–	–	–	3.6	–
Gypsum	–	–	–	–	–	–	–	3.6	–
X-ray-amorphous	22.4	60.0	57.1	62.3	70.8	88.5	74.0	–	–
Total	100	100	100	100	100	100	100	100	100
Hematite*	Total amounts increase by decomposition of Fe-hydroxyoxides								

EDX but could not be identified as wüstite. About 70 wt% of the sample was X-ray-amorphous.

SL consists of 88.5 wt% X-ray-amorphous phases and hibonite ($CaAl_{12}O_{19}$).

The FA reference is mainly X-ray-amorphous (74 wt%), containing mullite, quartz, calcite and hematite. The limestone is a pure calcite, while the OPC has a common clinker composition and gypsum content [42].

The reactivity of VBR and SL originates from their glassy phases, which were investigated using ATR-FTIR and Raman spectroscopy. Spectra and interpretation are included in the supplementary materials (Figs. S 3 to 4).

It was confirmed that the X-ray-amorphous phases in VBR and SL are glasses. The presence of major crystalline phases detected via XRD was confirmed. ATR-FTIR results showed that VBR is an alumosilicate glass, while SL has a very open aluminate glass structure. This explains the higher R^3 reactivity of SL compared to VBR (reported in [8]).

2.4. Preparation of anhydrous binders

Binders were prepared according to the formulations provided in Table 3. The blend identifiers combine SCM type and replacement level, while LS denotes limestone-containing blends.

Substitution levels of 10, 30 and 50 wt% SCM were investigated. In selected binders 5 wt% (COCBLS) and 15 wt% (VBRLS-systems) of limestone replaced additional OPC, resulting in clinker contents down to 35 wt% (VBRLS-50). Due to varying amounts of $CaSO_4$ addition, the binder compositions given in Table 3 slightly deviate from the targeted SCM contents. Corresponding to the EN 197-1 threshold (4.0 wt% SO_3), up to 3 wt% $CaSO_4{\cdot}2H_2O$ were added to the VBR, VBRLS and SL systems.

2.5. Preparation of paste samples

Pastes of water-to-binder ratio 0.4 were mixed using a paddle mixer (IKA Eurostar 60 Digital) stirring at 1600 and 2000 rpm for 1 min each. Superplasticizer (Glenium ACE 460, Master Builder solutions) was used to adjust the pastes flow spread to 60 ± 5 mm (mini-cone method [43]).

Table 3
Composition of studied binders, the bold entries were also used in mortar scale experiments.

Blend Name	Components in wt%			
	SCM	OPC	LS	Gypsum
OPC	**0.0**	**100.0**	**0.0**	**0.0**
FA-10	**10.0**	**90.0**	**0.0**	**0.0**
FA-30	**30.0**	**70.0**	**0.0**	**0.0**
FA-50	**50.0**	**50.0**	**0.0**	**0.0**
BR-10	**9.8**	**88.2**	**0.0**	**1.9**
BR-30	**29.4**	**68.6**	**0.0**	**1.9**
BR-50	**49.0**	**49.0**	**0**	**1.9**
COCA-10	9.8	88.2	0.0	1.9
COCA-30	**29.4**	**68.6**	**0**	**1.9**
COCA-50	49.0	49.0	0	1.9
COCBLS-10	9.8	83.3	4.9	1.9
COCBLS-30	**29.4**	**63.7**	**4.9**	**1.9**
COCBLS-50	49.0	44.1	4.9	1.9
COCB-10	**9.8**	**88.2**	**0.0**	**1.9**
COCB-30	**29.4**	**68.6**	**0.0**	**1.9**
COCB-50	**49.0**	**49.0**	**0.0**	**1.9**
COCC-10	9.8	88.2	0.0	1.9
COCC-30	**29.4**	**68.6**	**0.0**	**1.9**
COCC-50	49.0	49.0	0.0	1.9
VBR-10	**9.7**	**87.4**	**0.0**	**2.9**
VBR-30	**29.1**	**68.0**	**0.0**	**2.9**
VBR-50	**48.5**	**48.5**	**0.0**	**2.9**
VBRLS-10	**9.7**	**72.8**	**14.6**	**2.9**
VBRLS-30	**29.1**	**53.3**	**14.6**	**2.9**
VBRLS-50	**48.5**	**34.0**	**14.6**	**2.9**
SL-30	29.1	68.0	0.0	2.9

Fresh paste was cast into cylindrical silicone molds (25 × 100 mm), demolded, and cured in artificial pore solution as described in [44]. At hydration ages 1, 2, 3, 7, 28, 56, 90, and 180 d, 3–4 mm thick slices were cut (QATM Qcut 150 M) for analysis. If required, hydration was stopped by solvent exchange with isopropanol as described in [44]. After 7 d, the samples were vacuum-dried to constant mass and stored in an argon atmosphere.

3. Results

3.1. Compressive strength

Fig. 2 (a) plots the 180 d SAI of the standard mortars as function of the SCM content; the black line represents an ideal filler with negligible nucleation effects. Untreated BR shows a negative strength contribution across the complete substitution range, consistent with [16]. For FA, COCB, COCBLS and VBR, SAI decreases with increasing substitution level, and the SCMs impact on strength becomes visible at 30 to 50 wt% substitution, a range relevant for modern binders. At 30 wt% VBR, COCB and COCBLS achieve SAIs of 0.75–0.82, compared with 0.95 for the FA reference. At 50 wt% substitution FA, VBR, COCB and COCBLS converge at ≈0.7. In contrast the VBRLS system maintains a SAI above 0.8 across all replacement levels. It is a promising low-clinker system. The increased late age strength of limestone containing systems (COCBLS and VBRLS) indicates a synergistic interaction between modified BRs and limestone.

Fig. 2 (b) compares the 2 d (hatched bars) and 180 d (colored bars) SAIs of 30 wt% blended cements. FA and VBR exhibit the typical behavior of pozzolanic systems, with reduced early-age performance and increased late age strength. In contrast, blends containing zeolitic DSP phases (BR, COCA to COCC) show higher SAIs at 2 d than 180 d. The co-calcined BRs reach 2 d SAIs close to 1, suggesting a reactive contribution of DSP phases to early hydration. This is supported by the positive trend between DSP content and 2 d SAI (Fig. S 9), although further experiments are needed to establish a causal relationship. To further assess the reactive contribution of modified BRs, the evolution of their phase assemblages was investigated.

3.2. Phase assemblage evolution

To compare the phase assemblage evolution among 30 wt% blended cements between 1 and 180 d, Fig. 3 shows the (a) clinker degree of hydration (DoH) and the contents of (b) ettringite, (c) AFm, and (d) portlandite. Fig. A14 presents the cumulative phase assemblages of selected binders as stacked area plots, with dashed lines highlighting the experimental data points. Quantitative phase assemblages for all systems (10 to 50 wt% SCM content) are reported in tables S 10 to S 34, and were derived from Rietveld refinements with uncertainties similar to those of [45].

Fig. 3 (a) presents the evolution of the clinker DoH. Differences between binders become notable after 7 d. After 180 d OPC, FA-30 and VBRLS-30 reach a DoH of 94%, whereas VBR-, COCA- to COCB- and BR-30 reached 90 to 92%. SL-30 exhibited the lowest DoH (≈ 85%). VBRLS-30 reached a higher DoH than VBR-30, indicating an enhanced reactivity of VBR in presence of limestone, consistent with the higher compressive strength. Results for 10 and 50 wt% blends (Fig. A13) confirm that the late-age DoH of the sodium-rich systems (COCA-COCC, COCBLS, VBR, VBRLS and BR) decreases with increasing replacement level, consistent with [46]. The reduction between 10 and 30 wt% substitution was larger than between 30 and 50 wt% replacement and surpassed the variation among the COCBRs at a given replacement level, indicating that SCM content had a stronger effect on clinker hydration than BR source.

Fig. 3 (b) and (c) show the evolution of ettringite (AFt) and total AFm contents. They are discussed together. AFt partially converts to monosulfate (Ms) after sulfate depletion, when sufficient Ca and Al ions are

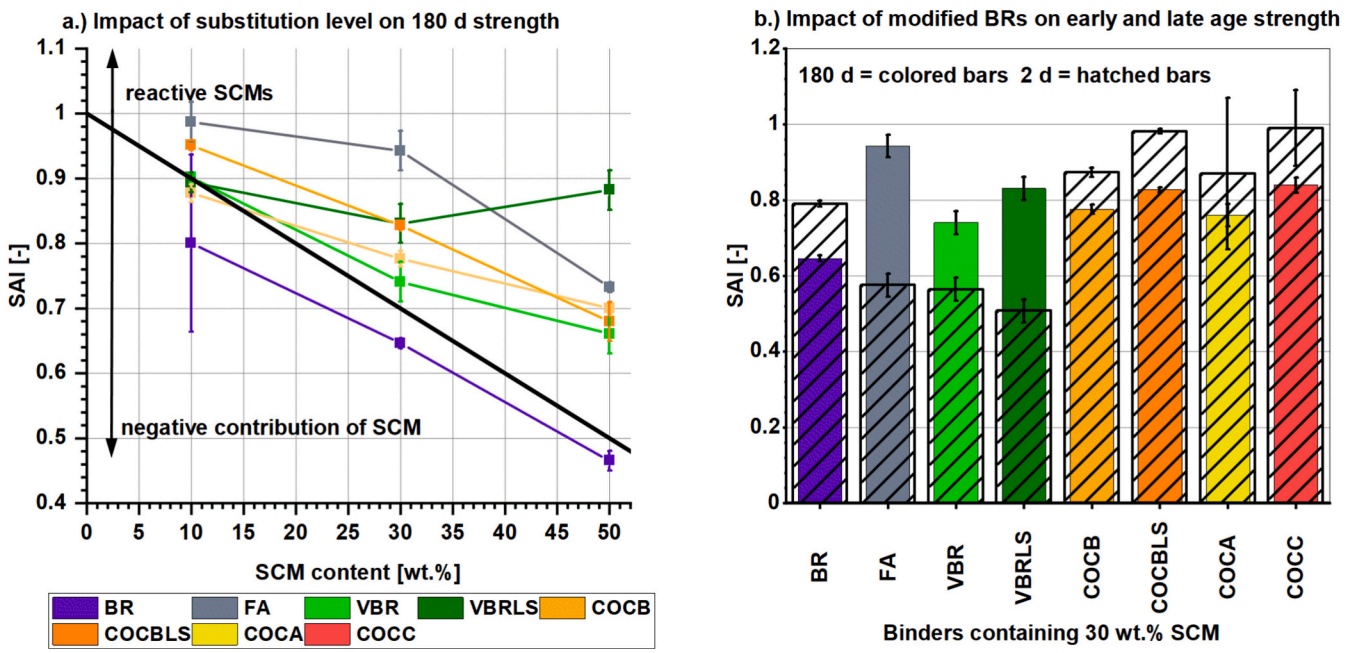


Fig. 2. (a) Plots the strength activity index of 180 d cured standard mortars as function of the SCM content. The black-line visualizes the SAI expected for an ideal filler that does not significantly boost hydrate nucleation. (b) Plots the 180 and 2 d SAIs of 30 wt% SCM containing binders to compare the SCMs contribution to early and late age strength.

available. In the presence of calcium carbonate, this conversion is suppressed because monocarbonate (Mc) is thermodynamically favored, resulting in elevated sulfate concentrations limiting AFt dissolution [47].

Fig. 3 (b) and (c) show the evolution of ettringite (AFt) and total AFm contents. They are discussed together. In OPC, FA-30, and VBR-30, AFt formed during the first 48–72 h and partially converted to monosulfate after sulfate depletion, leading to increasing AFm contents. Still nearly constant AFt contents (±2 wt%) were reached between 90 and 180 d. BR-containing binders generally formed more AFt and AFm than the reference systems. BR, COCA, COCB, and COCC (the zeolitic DSP containing materials) formed AFm within 24 h, compared to 48–72 h for OPC, FA, and VBR. In this context the detection of carboaluminate AFm in the VBRLS blends after 24 h requires further investigation. In the other BR blended cements an earlier AFm precipitation was always consistent with the dissolution of OH-sodalite and cancrinite. These crystalline DSP phases were depleted within 72 h in COCA and COCB (Fig. A14), while the reactive contribution of X-ray amorphous DSP phases could not be assessed and requires further investigation, as does the dissolution of the VBRs glassy phases. AFt decomposition was suppressed in limestone containing systems. SL-30 showed a unique reaction pathway, with rapid AFt formation (< 24 h) followed by AFm consumption and continuous strätlingite precipitation after CH depletion. This observation was consistent with [48] and might be attributed to SLs high aluminate content.

In SL-30 strätlingite precipitation occurred after CH depletion (≈48 h), accompanied by Ms. dissolution. The most plausible reaction pathway is described in Eq. (4) [48,49].

$$C_4A\bar{S}H_{12} + 1 \bullet SiO_2 + 0.5 \bullet Al_2O_3 \rightarrow 1 \bullet C_2ASH_8 + 0.5 \bullet C_4A\bar{S}H_{12} + 0.5 \bullet Ca^{2+} + 0.5 \bullet SO_4^{2-} \quad (4)$$

The open-structured, fine particulate Ca-alumosilicate glasses of SL-30 were highly soluble, explaining its early dissolution despite the SCMs low alkali content. The impact of modified BRs on the kinetics of AFm formation seems related to the dissolution of the Na and Al bearing phases of the SCMs which is further discussed in Section 3.2.1.

Fig. 3 (d) shows CH content over time. All blended cements exhibit notably lower CH contents than the OPC reference, while a decrease in CH content between 1 and 180 d was only observed for VBR-30, FA-30 and VBRLS-30. Because pozzolanic AFm formation consumes more Ca (≈0.4 g_{Ca}/g_{phase}) than pozzolanic C-A-S-H precipitation ($Ca_{1.5}Al_{0.2}SiO_{3.5}{\cdot}6H_2O$ ≈ 0.24 g_{Ca}/g_{phase}), Al-rich modified BR-blends consumed more CH than the FA references. Total CH consumption correlates with the R^3-reactivities of the modified BRs.

Modified BRs differ from conventional pozzolans by (1) causing a modest reduction in clinker DoH (<10%), (2) elevating CH consumption and aluminate hydrate formation and (3) altering AFm and AFt precipitation kinetics depending on the mineralogy of their Na bearing phases. The accelerated AFm precipitation in COCBR blends may contribute to their higher early-age strength compared with VBR binders, motivating further investigation of the early-age reactivity of these SCMs.

3.2.1. *Early-age kinetics*

Fig. 4 depicts the heat flow ((a) and (c)) and cumulative heat release ((b) and (d)) of cement pastes (30 wt% SCM) as a function of time. Both are normalized to cement content [65]. Subplots (a) and (b) compare BR-based slags, while subplots (c) and (d) compare COCBRs and the BR reference.

To ensure the compliance of modified BR blended cements with EN-197-1, their total SO_3 content was limited to 4.0 wt% [3]. Sulfate-optimized systems exhibit the expected heat flow sequence illustrated by VBR-30. The black numbers in Fig. 4 (a) correspond to (1) the silicate peak, (2) the aluminate peak, whose onset corresponds to sulfate depletion, and (3) an additional peak associated with high Al contents.

VBR-30, FA-30 and OPC were properly sulfated, exhibiting low and broad aluminate peaks (SDT ≈ 14 h) clearly separated from the silicate peak. In contrast, COCBR blends (Fig. 4 (c)) showed earlier (SDT ≈ 10–13 h), sharper, more intense aluminate peaks. These peaks occurred closer to the silicate peak maximum, despite comparable reactive Al contents, while the third peak was less pronounced than in VBR-30.

The early-hydration kinetics are affected by DSP chemistry. BR-30 and COCB-30 are based on the same BR, showing similar sulfate depletion times (≈12 h) and aluminate peak shapes. COCC-30 has an

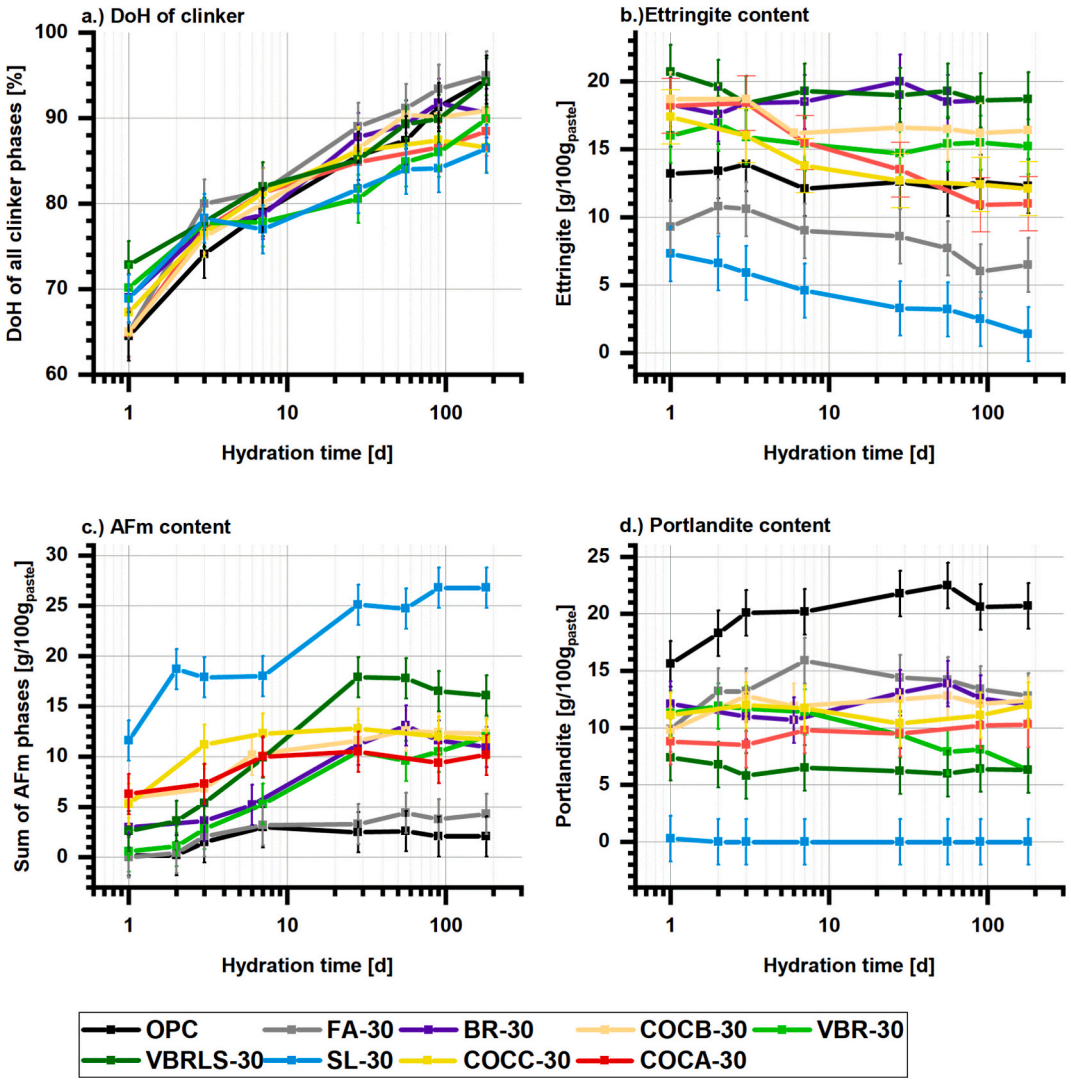


Fig. 3. Evolution of (a) clinkers degree of reaction, (b) ettringite, (c) AFm phases (strätlingite included) and (d) portlandite.

earlier, sharper aluminate peak (SDT ≈ 10 h). COCA-30 has a less visible aluminate peak (SDT ≈ 13 h) and the fastest silicate reaction among the COCBR systems. The increasing undersulfation is consistent with the increasingly fast dissolution of the zeolitic DSP (COCA-30 < COCB-30 < COCC-30). COCB-30 and COCC-30 exhibit an additional "AFm shoulder" around 1 d (Fig. 4 (c)), consistent with higher AFm contents. COCBR blended cements were more sensitive to sulfate adjustment but required slightly lower total sulfate contents than VBR blends (Table 3). This could be related to the faster dissolution of their zeolitic phases compared to the VBRs glassy fraction. Nevertheless, the COCBR blends remain sufficiently regulated to avoid flash-setting, suggesting a balanced hydration profile.

COCA-30 and BR-30 released less cumulative heat than other BR blends. A faster alkali release may have accelerated the DSPs dissolution processes, while limiting the silicate reaction at later ages, potentially due to surface sorption of Al species as reported in [50]. For COCA-30 this is consistent with a reduced maximum clinker DoH, agreeing with [46]. COCA-30 shows the highest SDT and the lowest compressive strength among the COCBR-30 blends, so undersulfation is unlikely to be the primary performance limiter in COCBR systems.

SL-30 (Fig. 4 (a)) displays a sharp aluminate peak preceding a small, broad silicate peak indicative of pronounced undersulfation. This is attributed to SL's high aluminate content (Table 1). Consistently, SL-30 developed an AFm-dominated microstructure containing notable amounts of strätlingite (see Fig. A14 (f)). Despite the maximum sulfate content of 4 wt% of SO_3, higher sulfate additions would be required for a sulfate adjustment of this system. Despite its low clinker DoH, SL-30 showed a cumulative heat release similar to other BR blended cements, associated with enhanced aluminate hydrate formation.

Fig. 2 (c), consistent with [20,40], indicates that dissolution of Na-alumosilicate phases in modified BRs, and the associated Na release, influence hydration kinetics and AFm precipitation in these systems. In COCBR blends, rapid dissolution of Na-bearing zeolites (Fig. A14) correlated with higher early-age strength than in VBR systems of equivalent SCM content (Fig. 2 (b)). In 30 wt% VBR containing mixes with comparable total alkali contents (Table 1), AFm precipitation occurs later (48–72 h), suggesting that the differences arise from the Na release rate of the SCM. The dissolution of the VBR glass resulted in less accelerated hydration and a slower strength development.

Fig. 5 compares the heat flow of blends containing 10, 30, and 50 wt % SCM, with and without limestone addition, normalized to OPC content (g_{cement}). The systems are grouped according to the SCM. Subplots (a) and (b), comparing COCB- and VBR-based blends, are discussed together to evaluate the influence of SCM content on hydration kinetics.

In isothermal calorimetry, nucleation effects appear as earlier and sharper silicate peaks, reflecting accelerated C_3S hydration. Filler addition was reported to accelerate AFt formation, increase sulfate consumption, and shift the aluminate peak to earlier times [51].

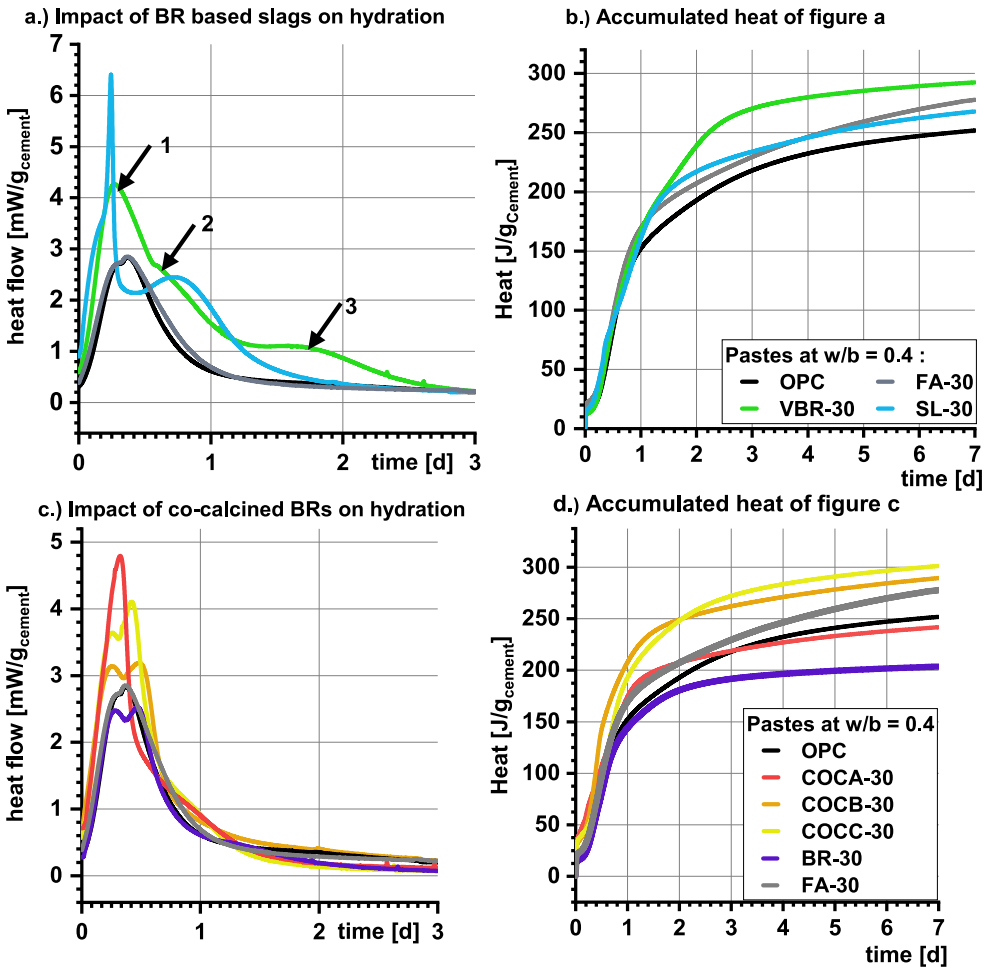


Fig. 4. Calorimetric study of 30 wt% substituted cement pastes. (a) Heat flow and (b) cumulative heat release of BR slag-blended cements; (c) heat flow and (d) cumulative heat release of cements containing untreated and co-calcined BRs. The numbered peaks in panel (a) correspond to (1) silicate reaction, (2) aluminate reaction and (3) SCM-related AFm formation.

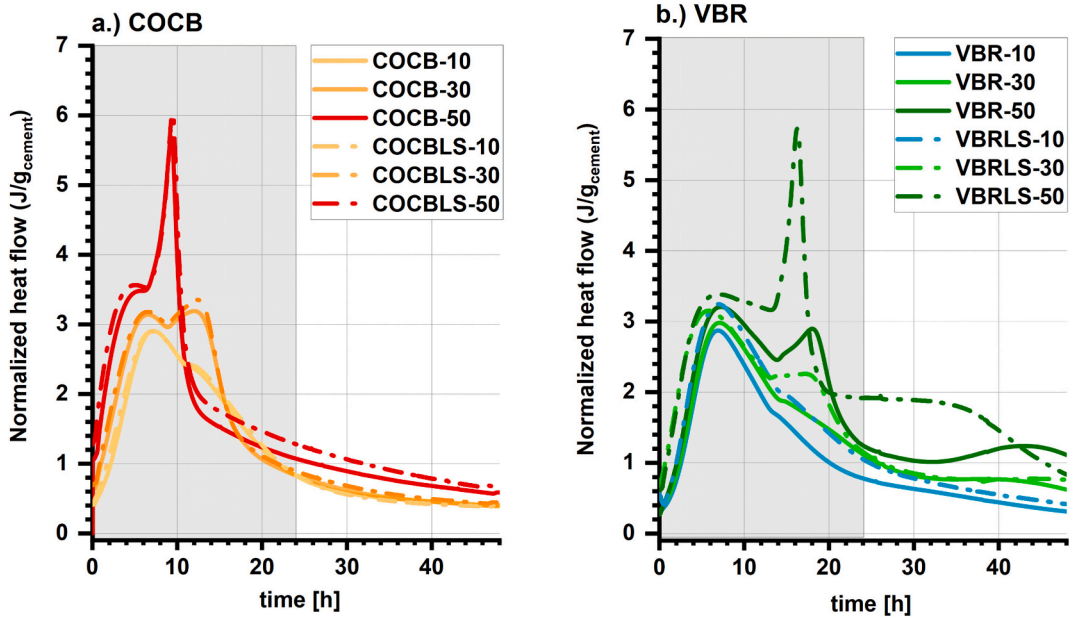


Fig. 5. Heat-flow curves of cement paste blended with (a) COCB and (b) VBR. The graphs outline the influence of replacement level (10–50 wt%) and limestone addition on hydration kinetics. Colors indicate the SCM replacement level, while solid and dotted lines denote binary and ternary binders, respectively.

Fig. 5 (a) shows that increased COCB addition led to earlier silicate peaks, whereas limestone addition had a negligible effect. This pronounced nucleation effect was consistent with the COCBRs high SSA (10–20 m^2/g) and fineness. In contrast VBR had a PSD and SSA comparable to OPC, resulting in minor changes in the silicate peak. Limestone addition (15 wt%) slightly advanced the silicate peak in VBR systems.

Enhanced aluminate hydrate formation was associated with increased sulfate demand in all modified BR blended systems. Accordingly, 50 wt% VBR and COCBR blends exhibited earlier and sharper aluminate peaks than their 30 wt% counterparts. Limestone intensified the undersulfation in VBR blends, consistent with enhanced nucleation and pozzolanic reaction. The nucleation effect of COCB likely contributed to their higher 2 d strength, but is not directly linked to earlier AFm precipitation.

The sulfate limited model system (SLiM test) [25] was used to decouple intrinsic early-age reactivity of the SCM from clinker hydration and dilution effects. This calorimetric test evaluates the dissolution of SCMs through the Sulfate-Carrier-Depletion-Time (ScDT) during their reaction with calcium and sulfate sources. Representative heat-flow curves are shown in Fig. A15. The SLiM methodology was developed by Muzenda and Demeusy [24,52] to evaluate the early-age reactivity of calcined clays by assessing their dissolution kinetics in the presence of cement hydrates and sulfate. Here, this method is applied on modified BRs.

The ScDTs are mainly related to the activation treatment. SL (SCDT ≈ 2 h) exhibited the highest reactivity, consistent with its open glass structure, followed by the COCBRs (ScDT = 3–12 h) and VBR (ScDT = 18–19 h). The ScDTs of VBR, COCB and BR fall within the range reported for kaolinitic clays (12 to 48 h), while SL, COCA and COCC dissolve faster [52]. The co-calcination of BR (ScDT ≈ 20 h) to COCB reduces the ScDT by ≈9 h indicating activation of both zeolitic DSP and kaolinite, consistent with the findings of Peys et al. [20].

Fig. 6 relates the relative slump reduction of cement paste after 30 min of hydration to the SLiM model systems' ScDT. Slump reduction increased with decreasing ScDT, indicating that faster SCM dissolution promotes structural build-up. This confirms the contribution of modified BRs to early hydration. Similar behavior was reported for calcined clays [52,53], which justifies the use of the SLiM system to classify the intrinsic reactivities of modified BRs. FA and quartz references showed no aluminate peaks in the SLiM test, consistent with their negligible early-age reactivity (Fig. A15).

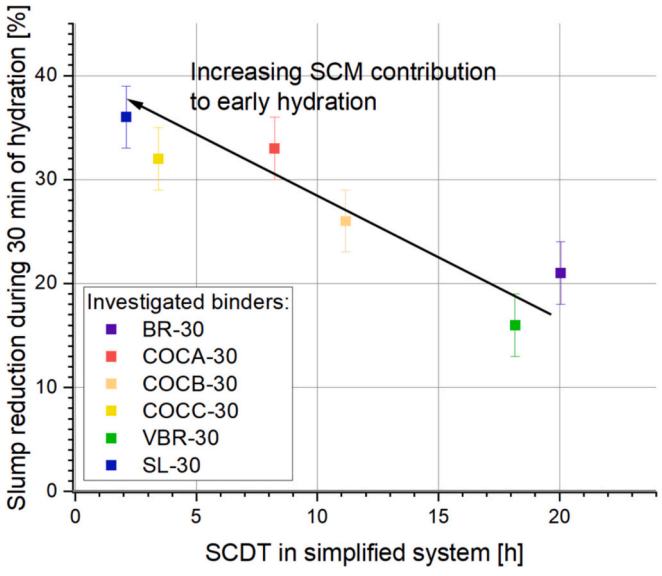


Fig. 6. Correlation of the SLiM tests sulfate carrier depletion time with the slump reduction of cement paste during the first 30 min of hydration.

Because the same kaolinite (99% purity, VWR, Bole White [20]) was used in all co-calcinations, differences in the COCBRs ScDTs primarily reflect variations in composition and amount of zeolitic DSP. COCC is dominated by crystalline OH-sodalite, COCB by cancrinite, and COCA by X-ray-amorphous DSP fractions. Although structural disorder in OH-sodalites can promote their transformation to cancrinite or nanocrystalline precursors [54–56], the high reactivity of COCC indicates that less structural disorder in crystalline DSP does not necessarily reduce its pozzolanic reactivity.

Modified BRs dissolved rapidly and impacted the structural-buildup of cement paste during very early hydration. Detailed studies of pore solution chemistry and phase assemblage evolution during the first hours of hydration are required to elucidate the role of their reactive phases on hydration kinetics.

3.2.2. *Pozzolanic activity over time*

Portlandite (CH) consumption is commonly used as an indirect measure of pozzolanic reactions. To separate CH consumption from dilution, the CH contents of blended cements were normalized using Eq. (2) (Section 2.2.3). This resulted in normalized CH (R_{CH}) values of 1 for OPC and 0 for a CH-depleted system. Fig. 7 (a) to (c) show the evolution of R_{CH} with hydration time, grouped by SCM content.

During early hydration several 10 to 50 wt% BR, COCBR VBR or FA blended cements exhibited R_{CH} values above 1, consistent with enhanced clinker hydration through nucleation or alkali-acceleration effects. All BR-derived systems reached RCH values below 1 after 72 h, indicating a pozzolanic CH consumption, whereas the FA blends reached this stage only after 28 d, consistent with [57]. At later age VBRLS-10 and VBR-10 exhibited a larger R_{CH} reduction than the 10 wt% COCBR, BR and FA blended systems. The particularly low R_{CH} of VBRLS-10 suggests a limestone – VBR synergy rather than a dilution effect. Despite having the lowest total CH consumption FA-10 continues to react across the investigated time period, while the BR blends approach stable values between 56 and 90 d. The stabilization indicates either a negligible pozzolanic reaction at later age or a dynamic balance between SCM reaction and clinker hydration.

Differences between the SCMs became more pronounced at 30 and 50 wt% substitution (Fig. 7 b to c). At 30 wt% substitution CH consumption increased in the order FA < COCA to COCC ≈ BR < VBR < VBRLS ≪ SL, consistent with the 50 wt% blended systems. With increasing substitution, the CH consumption persisted longer, mirroring the growing contribution of the SCM to hydration. Between 56 and 180 d BR, all COCBR and BR blends reached stable R_{CH} values. The R_{CH} variation between COCA-, COCB- and COCC-30 blends was comparable or greater than their difference to BR-30, suggesting a notable influence of BR source on the pozzolanic regime. Despite its negative impact on compressive strength, untreated BR blends showed notable CH consumption. This warrants a further investigation of its reaction pathways. R_{CH} stabilization was observed for VBR-30 and VBRLS-30, while the 50 wt% VBR blends consumed CH throughout the 180 d period. This indicated slower and more persistent reaction kinetics, similar to those of GGBFS blended cements [58]. Continuous CH consumption was observed for FA-30 and FA-50, consistent with [57]. These results showed that thermochemical modification of BR changed extent and duration of CH consumption.

To relate CH consumption with SCM reactivity, Fig. 7 (d) presents the CH content after 7 d as function of normalized R^3 reactivity (R^3 cumulative heat release multiplied with the binder's clinker factor). A normalized R^3 reactivity of 120 J/g_{SCM} corresponds to CH contents from 5 to 12.5 $g/100\ g_{paste}$, therefore the R^3 results do not directly correlate with CH content. The scatter is related to the chemical and mineralogical differences of the compared SCMs. However, each individual binder systems exhibits an approximately linear trend between 10 and 50 wt% substitution, suggesting a constant relative contribution of clinker hydration and SCM specific pozzolanic reactions across the investigated

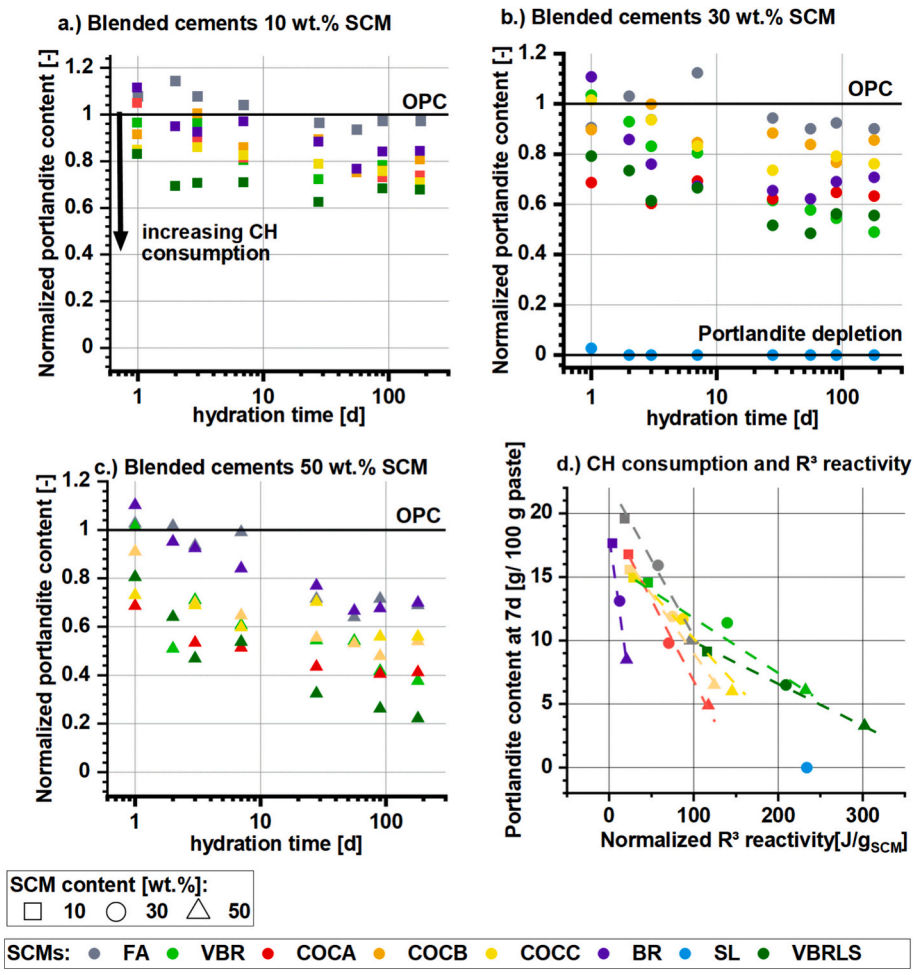


Fig. 7. (a) to (c) Development of normalized portlandite content from 1 to 180 d. The subplots are arranged according to substitution level. (d) Correlation between normalized portlandite content and normalized R^3 reactivity.

substitution range. These findings are consistent with [23].

Overall, Fig. 7 conveys four key points:

1. VBR exhibits a clear synergy with LS. The enhanced CH consumption is not related to dilution but to an increased SCM reactivity in ternary systems.
2. CH consumption of the blended systems increases in the sequence of their R^3 reactivity (co-calcination < vitrification ≪ reductive smelting).
3. Untreated BR shows a notable CH consumption despite its negative impact on compressive strength, indicating differing reaction pathways compared to COCBR blends.
4. Modified BRs are too diverse to directly relate R^3 results with portlandite contents. However, each system shows linear trends of both, implying a constant pozzolanic regime across the investigated substitution range.

3.3. Late-age phase assemblage

Section 3.3 focuses on the "late-age" microstructure and morphology of selected 30 wt% SCM containing blends.

3.3.1. Solid phases and bound water

Fig. 8 shows the simplified phase assemblages (a) to (c) and total bound water content (d) of the blended cements after 180 d of hydration. The phase assemblages are presented as stacked bar plots, grouped by SCM content and type. Phases were classified as (1) unreacted phases (residual clinker, Al-, Fe- and Ti-bearing phases), (2) crystalline hydrates (AFt, AFm, strätlingite), (3) X-ray-amorphous (amorphous anhydrous and C-A-S-H), (4) water-bound in X-ray amorphous and (5) free water. The total bound water contents are grouped by replacement level and SCM type.

The unreacted phase content increased with substitution level and was mainly governed by residual SCM phases. At 10 wt% substitution (Fig. 8 (a)), BR-10 and VBRLS-10 showed the highest unreacted fractions consistent with a lower clinker DoH and limestone addition, respectively. At 30 wt% replacement (Fig. 8 (b)), SCM chemistry becomes more pronounced, with unreacted phase contents decreasing in the sequence BR ≫ COCC > COCB = COCA > VBRLS > VBR = SL = FA. The same trend persisted, with higher absolute values, at 50 wt% replacement (Fig. 8 (c)). Thus, increased chemical modification and higher activation temperature reduced the inert phase content of modified BR blended cements.

The total crystalline hydrate content at 10 wt% SCM addition (Fig. 8 (a)) remains comparable across all systems. Trends emerge at 30 wt% replacement (Fig. 8 (b)), where the crystalline hydrate fraction increases in the order FA < OPC < COCA < COCB < COCC < BR = SL < VBRLS = VBR. The crystalline hydrate fraction (20 to 35 g/100g_{paste}) consisted mostly of portlandite and aluminate. The high AFt and AFm contents in 30 and 50 wt% modified BR blended systems increase the crystalline hydrate content. In contrast, Si-rich pozzolans like FA reduce the crystalline hydrate content. Consistently, FA-50 showed the lowest crystalline hydrate content among all systems.

The X-ray-amorphous content of 10 wt% blended cements decreased,

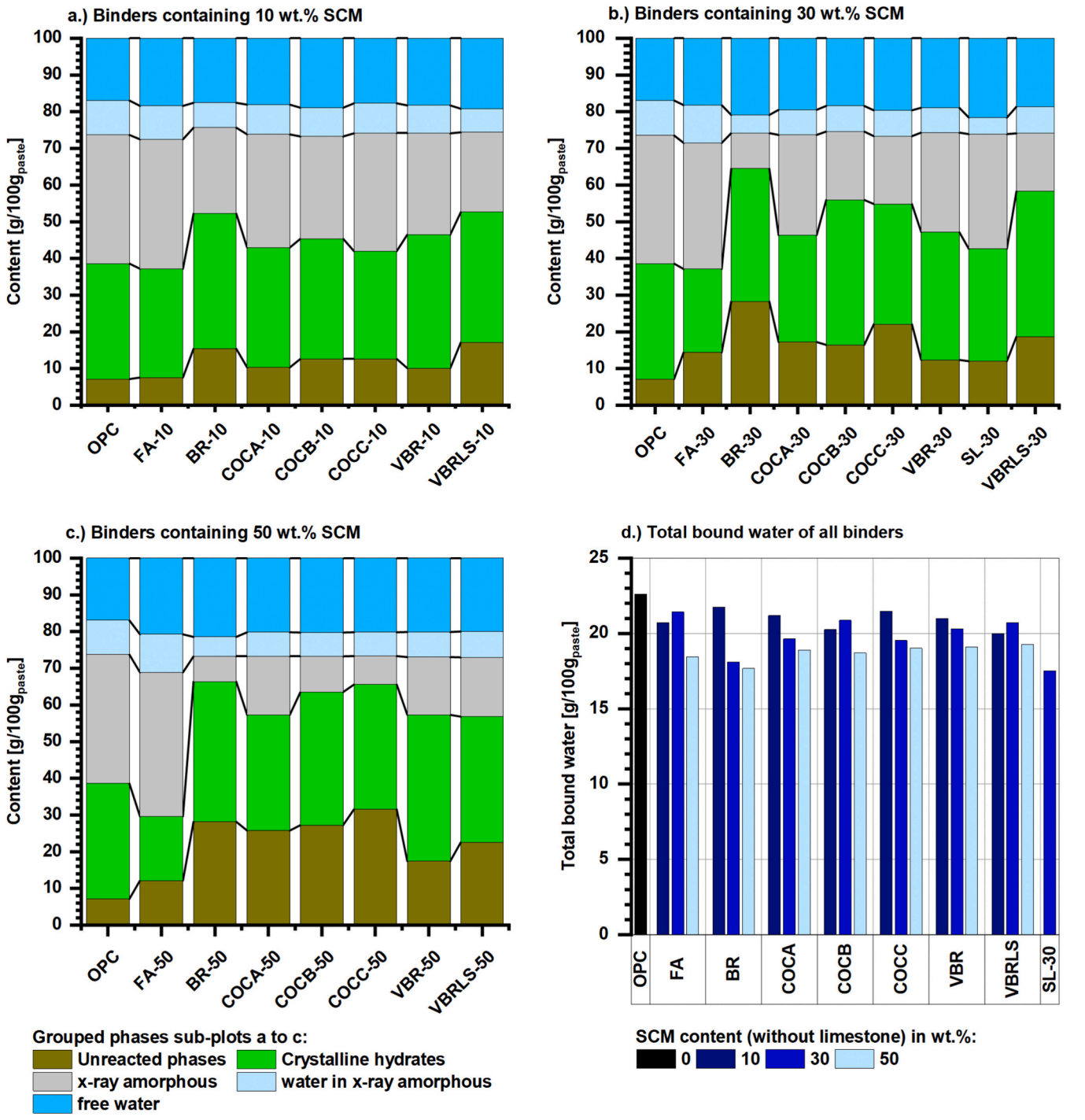


Fig. 8. (a) to (c) Simplified phase assemblages after 180 d of hydration, grouped according to SCM content. (d) Total bound water content of all investigated binders, classified following SCM type and replacement level.

consistent with the 30 and 50 wt% blended systems. At 30 wt% substitution the X-ray-amorphous content decreased in the sequence OPC = FA > SL > VBR > COCA >COCB = COCC > VBRLS > BR. This trend does not directly represent C-A-S-H contents, because SL, VBR and FA contain approximately 70 to 90 wt% X-ray amorphous phases, compared with approximately 60 wt% in the COCBRs and 20 wt% in BR. Nevertheless, the particularly low amorphous content of BR-30 may suggest reduced C-A-S-H formation, consistent with its mechanical performance (Section 3.1). At 50 wt% replacement (Fig. 8 (c)), FA-50 showed the highest amorphous content, reflecting both residual amorphous FA and pozzolanic C-A-S-H formation.

To obtain a proxy for C-A-S-H content, the anhydrous amorphous phases were separated from the water bound in X-ray amorphous phases, calculated as described in Section 2.2.3. At 10 wt% substitution (Fig. 8 (a)) FA-10 and OPC (9.6 g/100g_{paste}) exhibited the highest water content in the X-ray amorphous, whereas AFm- and AFt-rich modified BR blends showed lower values decreasing in the order COCC > COCA > COCB = BR > VBR > VBRLS. At 30 wt% replacement FA also exhibited higher X-ray amorphous water contents than the BR blends. VBRLS-30 was comparable to the COCBR blends, followed by VBR-30, BR-30. SL-30 exhibited the lowest value (4.7 g/g_{paste}), consistent with its predominantly AFm based microstructure. These trends persist at 50 wt%

replacement and FA-50 reaches the highest X-ray amorphous water content (10.8 g/g_{paste}), consistent with pozzolanic C-A-S-H formation.

Free water content primarily increased with the binders substitution level, consistent with literature trends [59]. At equivalent replacement levels, modified BR blends contained slightly more free water than the FA references. The highest values occurred in BR-30, BR-50 and SL-30. However, the scatter and uncertainty of the estimation (Section 2.2.3) prevents a more detailed interpretation.

Fig. 8 (d) summarizes the total bound water content of the cement pastes after 180 d. OPC shows the highest value (22.6 $g/100g_{paste}$), consistent with similar OPC paste assessed in [60]. Bound water content generally decreased with increasing SCM content, but no strict correlation was observed. This may be related to artefacts introduced during TGA sample preparation. For the modified BR systems, the decrease was more pronounced between 10 and 30 wt% than between 30 and 50 wt%. SL-30, BR-30 and BR-50 showed the lowest total bound water contents, consistent with the reduced degree of hydration of SL-30 and the low R^3 reactivity of untreated BR.

The key findings of Fig. 8 can be summarized as follows. Modified BRs increased dilution effects through their inert phase contents. In contrast to most blended systems (e.g. FA) the total proportion of crystalline hydrates in modified BR-blended cements is almost independent from replacement level. This reflects a change in hydrate assemblage, from high portlandite and low aluminate hydrate contents at 10 wt% SCM to high aluminate hydrate and low portlandite contents at 50 wt% SCM. Modified BR-blended cements are characterized by comparably low X-ray amorphous contents, which increase with the severity of the activation treatment. The lower amount of water bound in X-ray amorphous phases compared to FA references suggests a lower contribution of C-A-S-H precipitation in modified BR systems, although further investigation is required. Total bound and free water remained within a reasonable range for cement pastes (w/b 0.4). The total bound water contents do not strictly correlate with compressive strength, due to the differing hydrate assemblages among the systems.

3.3.2. *Morphology and X-ray-amorphous hydrates*

SEM-EDX mapping was used to assess the morphology and phase distribution of 28 d hydrated, 30 wt% modified BR blended cements through compositional phase maps (Fig. 9 (a) to (d)). Corresponding Al/Ca versus Si/Ca ratio plots and BSE images are provided in Fig. A18 and Fig. A17, respectively. Colored regions correspond to distinct phases, whereas grey areas could not be classified due to extensive phase intermixing. This is particularly important for C-A-S-H, which also occurs outside colored regions assigned to outer and inner C-A-S-H (magenta and blue).

Fig. 9 (a) shows the microstructure of BR-30, characterized by a heterogeneous matrix of nm- to µm-sized BR particles intergrown with C-A-S-H. Abundant, well-developed, AFm crystals, residual clinker grains (C_2S and C_4AF) and a large CH crystal were observed. Al- and Fe-rich particles of varying size are randomly distributed throughout the matrix. No anhydrous Na-rich particles were observed, indicating the complete dissolution of Na-bearing DSP phases and the dispersion of alkalis throughout the hydrate assemblage. This observation is consistent with QXRD results (Fig. A14), which demonstrate the complete dissolution of the zeolitic DSP during early hydration. Pore solution analyses of 90 d hydrated samples also reveal an SCM dependent increase of Na concentrations as discussed in the following section. By comparison, Na-rich agglomerates reportedly cover 10 to 30% of the surface area of anhydrous BR [61,62].

Fig. 9 (b) shows the microstructure of COCB-30. Large AFm crystals and CH particles are embedded in a C-A-S-H matrix. Residual SCM occurred mainly as compact multiphase agglomerates of 20–100 µm diameter. Unreacted Fe- and Al-rich particles were present and one Na-alumosilicate particle, likely zeolitic DSP, was identified. No alkali-rich hydrate rims were detected around the SCM agglomerates indicating the dispersion of the SCMs' Na throughout the hydrate assemblage, consistent with Section 3.3.3. Residual C_3S, C_2S and C_4AF grains were also observed.

The comparison of Fig. 9 (a) and (b) leads to three conclusions:

1. Co-calcination does not significantly affect AFm morphology.
2. Residual clinker grains are smaller in COCB-30, consistent with its higher DoH.
3. A heterogeneous microstructure containing agglomerates of anhydrous SCM is typical for COCBRs.

Fig. 9 (c) shows the microstructure of VBR-30. The sample contains a dense and homogeneous C-A-S-H matrix with numerous AFm crystals. Residual C_2S, C_4AF, CH particles and unreacted polyhedral slag particles were present. The overall morphology resembles that of GGBFS blended cements [63]. The residual slag grains contained Na-rich alumosilicate glass with polygonal magnetite inclusions and Fe-rich dendrites ranging from 100 nm to 1 µm (Section 2.3). After 28 d, the slag particles retain higher Na concentrations than the surrounding hydrates. This is consistent with a, compared to Na bearing zeolites in COCBRs, slower dissolution of the VBRS glass (Section 3.2.1). The importance of Na release rate for porosity refinement in modified BR blends requires further investigation. No distinct reaction rims were resolved around the slag particles, which could be related to a lack of immobile trace elements (e.g. Mg) in the glass phases.

Fig. 9 (d) shows the microstructure of SL-30. The matrix was dominated by sulfate-bearing AFm phases intergrown with strätlingite. C-A-S-H was also observed. Undersulfation (see Section 3.2.1) may promote an intergrowth of C-A-S-H with C-A-H phases, explaining the very high Al/Si- and Ca/Si-ratios of the C-A-S-H regions (Table 4). Consistent with TGA results (0.2 to 0.5 wt% CH at 28 d) only a few, small CH particles (<10 µm) were detected. Large residual clinker particles (C_3S, C_2S, C_4AF) confirmed the low DoH (Fig. 3 (a)) of SL-30. No residual slag particles were identified. This suggests extensive SL dissolution within 28 d, although complete dissolution cannot be confirmed due to the slag's low particle size (Fig. S 6).

Modified BRs primarily changed the amount and composition of AFm and C-A-S-H phases. Semi-quantitative elemental ratios of these phases are summarized in Table 4 and discussed by phase following the table columns. The AFm's ratios were normalized to Al, while those of C-A-S-H were normalized to Si.

Most modified BRs AFm Ca/Al ratios (2.0–2.5 ± 0.3) slightly exceed the ideal ratio (≈2.0) of sulfate and carbonate AFm [64] and likely reflect the experimental uncertainty of the method. BR-30 exhibited a Ca/Al ratio of 2.2 ± 0.5, while SL-30 showed a lower value of 1.7 ± 0.3 caused by the intergrowth of monosulfate (Ca/Al = 2.0) and strätlingite (Ca/Al = 1.0 [65]) (Section 3.2). The AFm phases (Na + K)/Al ratios increased in the sequence FA-30 < SL-30 < COCB-30 < COCC-30 < VBR-30 < BR-30. However, their compositions did not approach U-phase stoichiometry ($Ca_4Na_{0.5}(Al_{1.8}O_{2.7})1.1(SiO_2)\cdot 16H_2O$). The U-phase is a rarely observed AFm phase, in which Ca is partially substituted by Na [66,67]. The AFm phases of COCB-30, COCC-30 and BR-30 contained more Fe than those in SL-30 and FA-30 (0.06 ± 0.05). VBR-30 had the most Fe-rich AFm phases (Fe/Al = 0.3 ± 0.1), likely attributed to the higher availability of Fe^{2+} in VBR [21].

The C-A-S-Hs elemental ratios (Table 4) varied with SCM type. BR-30 showed a Ca/Si ratio of 1.7 ± 0.2, comparable to FA-, COCB- and COCC-30 (all 1.9 ± 0.2). VBR-30 reached a slightly higher value of 2.1 ± 0.2. All values fell within the reported range for C-A-S-H, except SL-30. This system showed an abnormally high Ca/Si ratio of 2.9, associated with intermixed Al-rich phases. This phase could be a mixture of C-A-H and C-S-H phases and requires further characterization. When Al incorporation is considered, the resulting Ca/(Si + Al) ratios of modified BR blended cements (1.8–2.0) fall into the range of OPCs [68,69]. The Al/Si ratios of C-A-S-H in modified BR-blended cements were comparable to those reported for LC^3–50 binders containing metakaolin-rich calcined clays [70]. The Na-rich systems C-A-S-H also had higher (Na + K)/Si ratios,

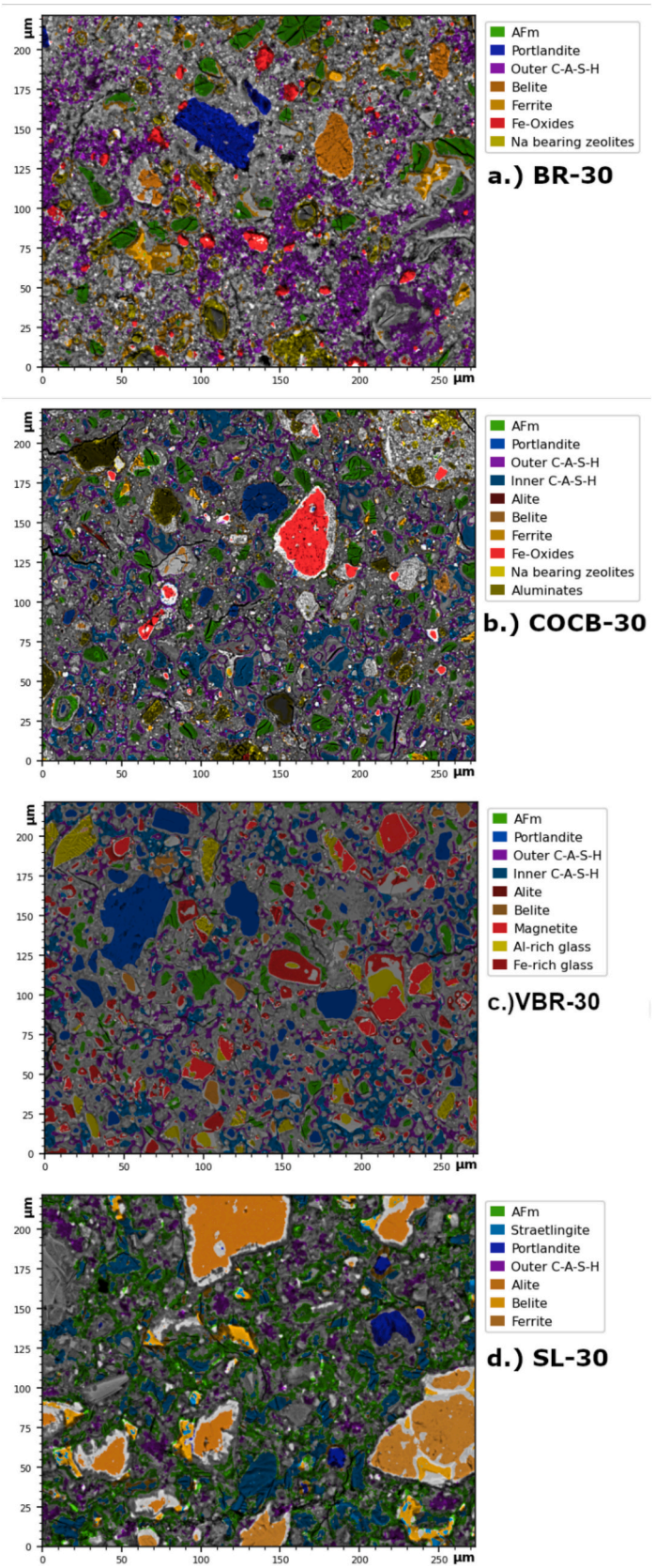


Fig. 9. Phase maps based on SEM-EDX mappings and subsequent data processing using EDXIA [11] after 28 d of hydration. (a) BR-30, (b) COCB-30, (c) VBR-30, (d) SL-30.

Table 4
Important element ratios for AFm and inner C-A-S-H phases of 28 d hydrated binders. For each dataset the scatter was obtained directly from the EDXIA plugin ($n < 500$).

Element ratios of AFm phases [at.%]				
Sample	Ca/Al	Si/Al	(Na + K)/Al	Fe/Al
BR-30	2.2 ± 0.5	0.3 ± 0.1	0.20 ± 0.04	0.17 ± 0.09
COCB-30	2.5 ± 0.3	0.3 ± 0.1	0.06 ± 0.02	0.14 ± 0.08
COCC-30	2.0 ± 0.1	0.5 ± 0.1	0.09 ± 0.06	0.16 ± 0.1
VBR-30	2.2 ± 0.3	0.4 ± 0.1	0.10 ± 0.02	0.3 ± 0.1
SL-30	1.7 ± 0.3	0.9 ± 0.1	0.05 ± 0.03	0.06 ± 0.05
FA-30	2.2 ± 0.3	0.3 ± 0.1	0.07 ± 0.1	0.03 ± 0.09

Element ratios of "C-A-S-H" phases [at.%]				
Sample	Al/Si	Ca/Si	(Na + K)/Si	Fe/Si
BR-30	0.31 ± 0.05	1.7 ± 0.2	0.34 ± 0.05	0.5 ± 0.3
COCB-30	0.28 ± 0.07	1.9 ± 0.2	0.05 ± 0.01	0.2 ± 0.2
COCC-30	0.30 ± 0.07	1.9 ± 0.1	0.13 ± 0.03	0.3 ± 0.2
VBR-30	0.44 ± 0.07	2.1 ± 0.2	0.13 ± 0.04	0.4 ± 0.2
SL-30	0.56 ± 0.09	2.7 ± 0.2	0.08 ± 0.01	0.18 ± 0.03
FA-30	0.17 ± 0.06	1.9 ± 0.2	0.08 ± 0.04	0.06 ± 0.02

indicating partial alkali incorporation as reported in [71]. The C-A-S-H in VBR-30 additionally contained more Fe than the other blends.

SEM-EDX phase maps showed dense microstructures containing C-A-S-H, AFm, and CH, together with residual clinker and, in most systems, unreacted SCM particles. The observed phases are consistent with the phase assemblages discussed in Section 3.2 and reveal that, compared to FA-30 and OPC, BR-based SCMs change the composition of C-A-S-H and AFm. The hydrates resemble those reported for aluminate-rich, calcined clay-limestone systems, but contain higher Na and Fe concentrations. Among the investigated systems the morphologies and phase assemblages of COCBR-30 and VBR-30 were closest to conventional blended cements.

3.3.3. *Pore solution analysis*

Pore solutions (PS) were analyzed after 90 d of hydration to complete the microstructural assessment. Because the hydrate assemblages changed minimally between 90 and 180 d, these data can complement the 180 d phase assemblages. Fig. 10 shows selected ion concentrations (Ca, Na, Al, pH) grouped by SCM type and substitution level. The concentrations of Si, Fe, K and SO_4 are provided in Fig. A16.

Fig. 10 (a) shows that Ca concentrations decreased with increasing SCM content. Systems richer in Al (SL-30) or Na (other BR-blended cements) exhibited the lowest Ca concentrations. In Na-rich systems this trend is consistent with the pH increase, which reduces Ca^{2+} solubility (Fig. 10 (d)). The low Ca^{2+} concentration of SL-30 agrees with its CH depletion (Fig. 3). At 10 wt% SCM, Ca concentrations decreased in the sequence OPC > FA > COCA to COCC > VBR. At 30 wt% SCM COCBRs and VBRs had comparable Ca^{2+} concentrations, while BR-30 and SL-30 exhibited lower concentrations. At 50 wt% FA-50 retained a notably higher Ca^{2+} concentration than the BR-blends. The pH of BR, VBR and COCBR blends increased at 30 and 50 wt% substitution (Fig. 10 (d)), whereas the pH of FA blends decreased as expected [72].

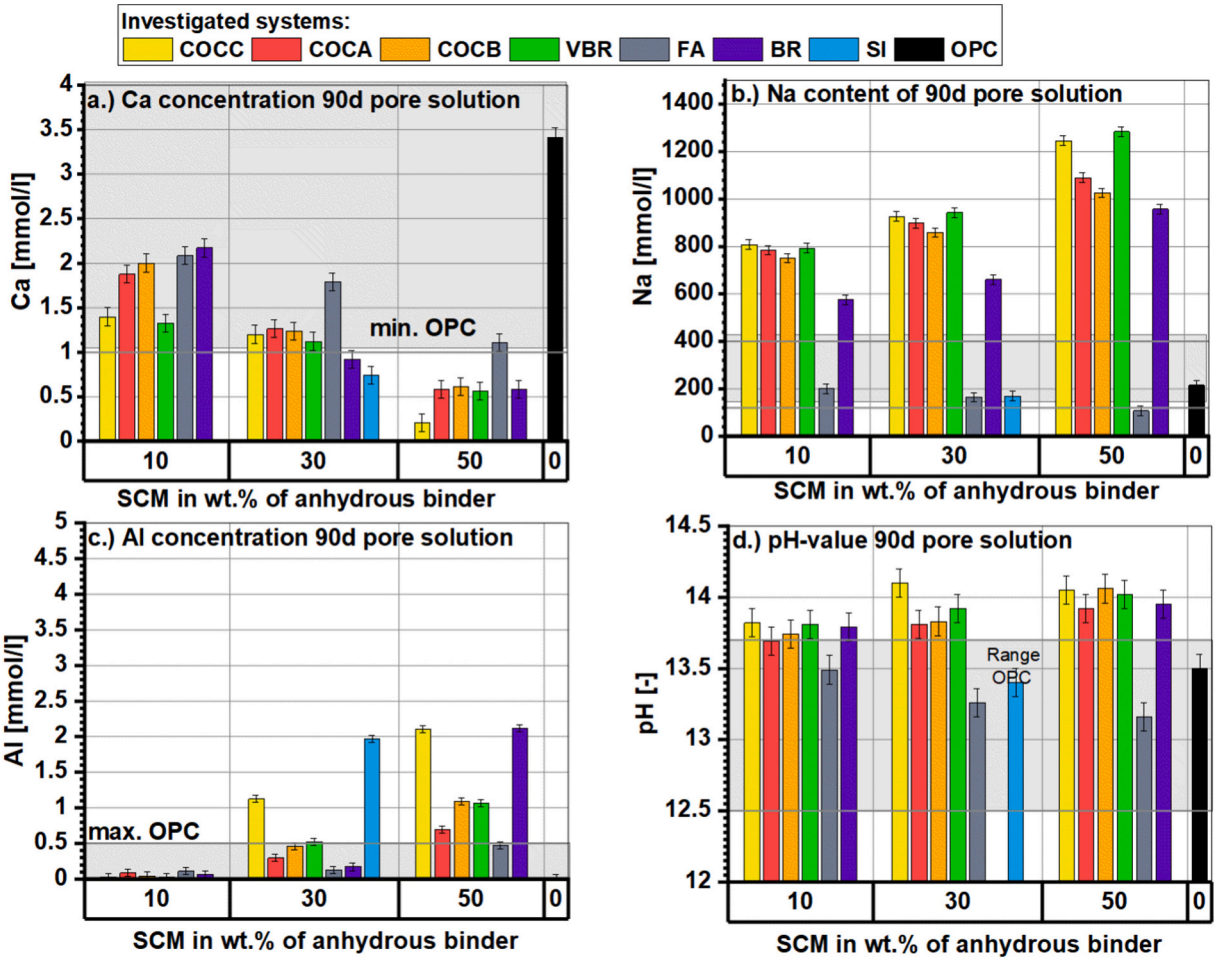


Fig. 10. Pore solution composition after 90 d of hydration: (a) Ca concentration, (b) Na concentration, (c) Al concentration and (d) pore solution pH. Due to the low volume of extracted pore solution, pH could not be measured for BR-30. The grey shaded areas represent the range of values reported for OPC in [72,73].

Fig. 10 (b) shows that Na concentrations decreased with FA or SL addition but increased with the addition of COCBR, BR and VBR, consistent with the Na contents of the SCMs (Table 1). At 10 and 30 wt% substitution, no significant differences were observed among the Na-rich binders. At 50 wt%, Na concentrations increased with the order COCB < COCA < COCC, following the DSP content of the COCBRs. This suggests that the BRs zeolitic phases control the Na concentration on pH of the pore solution. VBR-50 had the highest Na concentration. The K concentration correlated with OPC content (Fig. A16 (d)).

Fig. 10 (c) presents the Al concentrations. Differences between the SCMs became apparent at 30 wt% replacement. Al concentrations increased in the sequence: OPC < FA < BR < COCA < COCB < VBR ≪ COCC ≪ SL. COCC-30 and COCC-50 retained OH-sodalite after 90 d and exhibited higher Al concentrations than the other COCBR systems.

Fig. A16 summarizes the Si, Fe and SO_4^{2-} concentrations in the pore solutions. The Si concentrations of all blended systems were higher than in OPC, with the highest values measured for SL-30 and BR-50. Fe concentrations exceeded the OPC range [73] in BR-50, COCBR-50, and VBR-50. VBR blends showed the highest Fe concentrations, due to Fe^{2+} being the dominant species in VBR [21,74]. SL-30 showed particularly high silicate concentrations. This may be related to its aluminate-hydrate-rich phase assemblage but requires further investigation. All BR-based systems at 30–50 wt% replacement displayed elevated SO_4^{2-} concentrations, whereas FA systems remained within the OPC range [72]. This trend is consistent with the pH-dependence of sulfate sorption [72]. Overall, the elevated pH of BR-blended cements was associated with higher Na, K, Si, Al and Fe concentrations and reduced Ca concentrations.

Saturation indices (SIs) were calculated to relate pore solution chemistry to phase assemblage. Results for blends with 30 wt% SCM are presented in Table 5, those for 10 and 50 wt% blends are provided in Tables S 36 and 38. Calculated and measured pH values deviate by less than ±0.3 pH units, and no manual charge-balance correction was required for model convergence. All identified hydrates (Section 3.2) were either oversaturated or within ±0.05 of equilibrium, confirming consistency between pore solution composition and phase assemblages.

Compared to OPC, the Na-rich systems (excluding VBR-30 and COCA-30) exhibited greater oversaturation of AFt and AFm phases. Relative to FA-30, they also showed greater oversaturation with respect to monosulfate and, at 50 wt% substitution, OH-AFm. Despite the elevated pH, no destabilization of sulfate AFms was predicted [76,77]. Strätlingite was undersaturated in most modified BR blends but approached saturation with increasing aluminate and silicate concentrations, reaching near-equilibrium in BR-50 (SI = 0.007) and oversaturation in SL-30 (SI = 0.17). These results align with the QXRD and SEM-EDX analyses.

All binders were oversaturated with respect to the C-S-H endmembers, with BR-50 and SL-30 exhibiting the lowest saturation indices. Jennite was the dominant C-A-S-H endmember, consistent with the Ca/Si ratios determined via SEM-EDX. The relative contribution of the tobermorite endmember increased with SCM content. However, the calculated variation of C-A-S-H endmembers was smaller than expected. This could reflect the inability of the jennite - tobermorite C-S-H model to describe Al incorporation and alkali sorption in C-S-H.

Thermodynamic modeling predicted X-ray-amorphous ferrihydrite in all systems, while no experimental evidence of ferrihydrites was found. This discrepancy likely reflects the strong dependence of ferrihydrite supersaturation on Fe solubility. Si- ($C_3FS_{1.34}H_{3.32}$), Fe- ($C_3FS_{0.84}H_{4.32}$) and Al-hydrogarnets (C_3AH_6) were also predicted in all systems. After 365 d, X-ray diffractograms of VBR-50 and COCB-50 showed broad, low-intensity reflections near the expected (211), (220) and (311) reflections [78] of Fe/Si-hydrogarnets (see Fig. S 11). These findings are consistent with hydrogarnet formation, but no additional methods besides QXRD confirmed hydrogarnet precipitation. Pure Al-hydrogarnet is likely kinetically inhibited [78], so Fe-hydrogarnets are expected to form at room temperature [79] but could not be quantified. Further characterization of COCB-50 and VBR-50 by the SEM-EDX approach of Georget et al. [80] is ongoing. All experimentally detected hydrate phases in the 180 d phase assemblages are thermodynamically consistent with the measured pore-solution compositions.

4. Discussion

The main novelty of this study is the 1st quantitative dataset on phase assemblage evolution and pore-solution composition of blended cements containing up to 50 wt% of untreated, co-calcined, vitrified or reductively smelted BR. The results explain the good early-age performance reported for some BR-blended systems [17,81] and show how increased alkali concentrations alter the hydration pathways of alumina-rich blended cements. The distinct effects of modified BRs on hydration and compressive strength are discussed below.

4.1. The impact of bulk composition and mineralogy

Fig. 11 shows 180 d compressive strengths as function of the blends $CaO/(SiO_2 + Al_2O_3)$ ratio. The dashed line represents ideal dilution of

Table 5
Calculated saturation indices (SIs) of hydrate phases in pore solutions of 30 wt% SCM blended cements. Phase definitions and nomenclature follow [75]. Measured and calculated pore solution pH values are reported.

Main hydrates	OPC	FA-30	BR-30	COCA-30	COCB-30	COCC-30	VBR-30	SL-30
Saturation Indices [−]								
Ettringite	1.46	2.00	0.35	1.17	1.73	1.73	1.13	1.97
Monosulfate (14)	0.16	0.54	−0.04	0.98	1.42	1.43	1.23	1.37
OH-AFm (C_4AH_{13}))	−0.96	−1.17	−1.26	0.17	0.54	0.55	0.51	−0.30
Strätlingite	−3.62	−1.64	−2.21	−1.73	−1.35	−1.35	−1.14	0.17
Portlandite	0.96	0.42	0.47	0.76	0.76	0.76	0.74	0.03
Jennite * ($(CaO)_{1.67}(SiO_2)_1(H_2O)_{2.1}$)	2.42	4.09	1.76	2.46	2.35	2.38	3.43	1.34
Tobermorite II * ($(CaO)_{0.83}(SiO_2)_1(H_2O)_{1.33}$)	0.06	0.27	0.11	0.08	0.08	0.08	0.12	0.19
Ferrihydrite-am	−2.39	−2.03	−2.32	−2.47	−2.33	−2.33	−2.04	−2.33
Ferrihydrite-mc	0.62	0.98	0.70	0.55	0.65	0.70	0.98	0.68
Hydrogarnet phases								
$C_3FS_{0.84}H_{4.32}$	5.03	5.07	4.27	4.58	4.87	4.85	5.51	3.43
$C_3FS_{1.34}H_{3.32}$	3.89	4.49	3.48	3.62	3.88	3.88	4.64	2.93
Katoite (C_3AH_6)	0.01	0.08	0.07	0.96	0.11	2.3	2.3	1.46
Charge balance								
pH measured	13.5	13.3	–	13.8	13.8	14.1	13.9	13.4
pH calculated	13.6	13.2	14.0	14.0	13.8	14.0	14.1	13.6

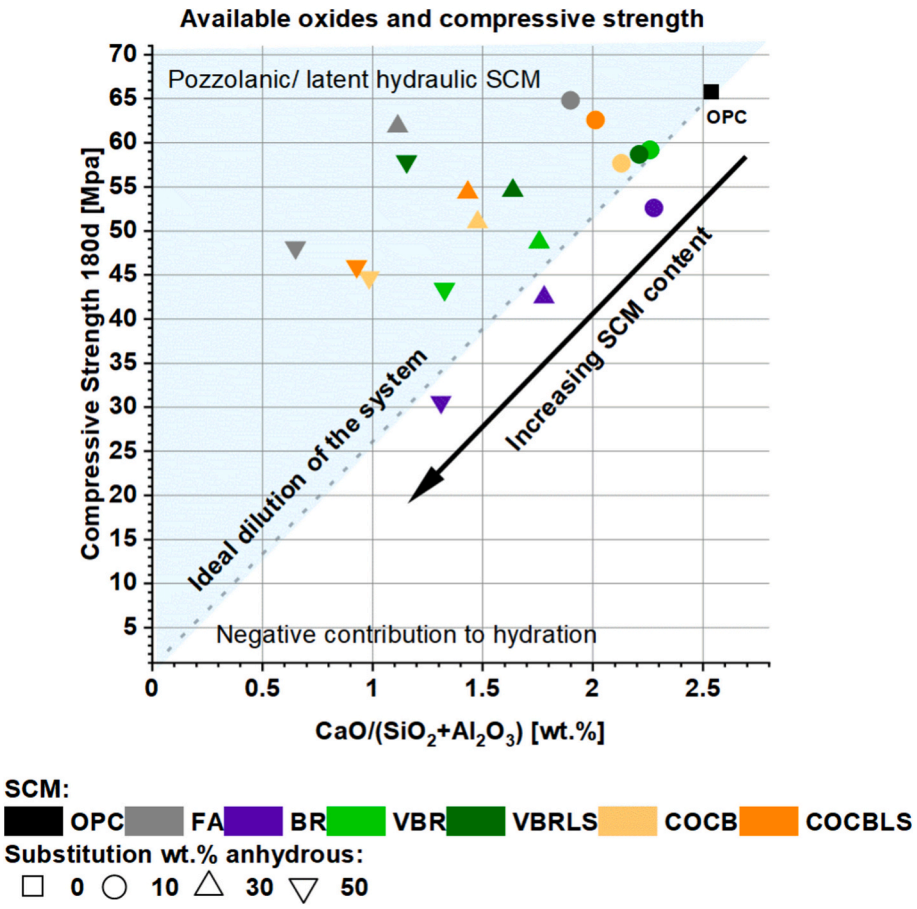


Fig. 11. Dependency of 180 d compressive strength on bulk chemistry as represented by the $CaO/(SiO_2 + Al_2O_3)$ ratio. Inert fillers like limestone or quartz have been excluded from the oxide contents.

the OPC reference without filler effects. The $CaO/(SiO_2 + Al_2O_3)$ ratio was calculated from the blends XRF (Table 1 and Table 3) after subtracting oxides associated with limestone and quartz (Table 2 and Table 3). The Strength clustered primarily by substitution level, indicating that clinker factor and Ca availability govern late age strength, as expected for pozzolan blended cements [82]. Differences between the SCMs were nevertheless apparent at 10 wt% substitution, despite the relatively similar bulk compositions of these binders. This confirms that mineralogy notably affects the pozzolanic contribution of the investigated SCMs, consistent with [8,20].

At similar $Ca/(SiO_2 + Al_2O_3)$ ratios compressive strengths differed by up to 30 MPa, indicating that the SCMs mineralogy affects strength in the same order of magnitude as the blend's bulk chemistry. For most SCMs, strength decreased linearly with substitution. This suggests a roughly constant balance between clinker hydration and pozzolanic reaction across the investigated composition range, supported by (Fig. 7 (d)). FA and VBRLS deviated from this trend. For FA-50 an increased strength loss was observed, consistent with a limited contribution at high FA contents [83]. In contrast the VBRLS-50 binder exceeded the expected trend, suggesting an increased slag dissolution at elevated pH [84]. Limestone addition increased the compressive strength of COCBLS and VBRLS systems. VBRLS blends maintain almost constant strength from 10 to 50 wt% substitution, making them the most promising low-clinker cement system in this study.

This performance is partially related to the VBRs higher Ca content (Table 1), which pushes the composition of the reactive phases closer to latent hydraulic SCMs and allows for higher replacement levels in a C-A-S-H dominated microstructure.

Fig. 11 highlights the importance of activation treatments for BR valorisation in blended cement. Untreated BR reduces late age strength across the full substitution range, likely due to its low reactive phase content and rapid Na release during early hydration (Section 3.2, and results of [46]). The limited Ca and Si availability in BR-blended systems may reduce C-A-S-H amounts (indicated by Fig. 9), whereas higher Al-contents increase AFt and AFm formation. FA systems compensate for low Ca availability by reducing the Ca/Si ratio in C-A-S-H at late-age, proving the importance of SCM choice for tailoring the mechanical and chemical performance of cements.

Fig. 11 shows that SCM performance cannot be assessed from bulk chemistry alone. SCM reactivity and resulting phase assemblage need to be considered to control strength development and environmental compatibility [20,85]. The present dataset provides a basis for developing thermodynamic models for modified BRs and BR-blended cements.

4.2. *Important factors for early-hydration in BR-blended cements*

Modified BRs influence early hydration through; (1) the nucleation effects of fine SCM particles and (2) SCM-derived Na, Al and Si release. The nucleation contribution of modified BRs varies with the activation treatment (Fig. 4). COCBRs and BR contain nm- to µm-sized particles with high specific surface areas (Table 1) [9,61], providing abundant nucleation sites that promote fast hydrate precipitation and strength development [17,20]. The coarser VBR slag provides fewer nucleation

sites, consistent with slower early hydration. Limestone addition shows the strongest synergies in VBR-rich systems, in line with the mechanisms described by Berodier et al. [51].

Pore solution pH controls the solubility of clinker phases and hydrates and is an important parameter in cement hydration. In cementitious systems, pH is controlled by dissolved alkalis and equilibria with the hydrate assemblage. For modified BR blends, pore solution data (Fig. 10) show that pH is primarily driven by substitution level and the SCMs Na content. Higher pH coincides with increased K, Na, Si, Al and Fe concentrations and reduced Ca concentrations, consistent with [86].

Mota et al. studied Na_2SO_4 and NaOH addition to white Portland cement at Na concentrations of 725 to 1450 mmol/L, comparable to the 650 to 1280 mmol/L measured here [46]. Their results align with this dataset: elevated Na concentrations accelerate silicate and aluminate hydration, increase early-age strength and slightly reduce the late-age clinker DoH. In both studies, the hydrate assemblages remained typical for blended cements and AFt was not destabilized. Mota et al. attributed AFt stability to elevated SO_4^{2-} concentrations, also observed here (Fig. A16). While the C_3S model system indicates that alkali uptake by C-A-S-H can change morphology and water content without substantially reducing mechanical strength [87], these findings need to be verified for alkali-rich blended cements. In modified BR blended cements, the water content of the X-ray amorphous fraction decreases with SCM content. This cannot be solely attributed to structural changes in C-A-S-H. Modified BR contents up to 30 wt% were associated with accelerated early hydration without notable loss of late age strength relative to the corresponding dilution trend. This contradicts studies that used similar amounts of NaOH as alkali accelerator [13,46] and requires further investigation.

The comparison of VBR and COCBR blends shows that Na-release rate, rather than Na content, control early clinker hydration and pozzolanic reaction. OH-sodalite and cancrinite (zeolites present in COCBRs and untreated BR) act as solid alkali accelerators and promote rapid AFm precipitation within the first 24 h (Fig. A14, Fig. 3 (c)). This behavior was rarely reported and may reflect the unusually high Al availability in these binders [46]. Incongruent dissolution of zeolitic DSP, initial cage ion exchange followed by framework dissolution or transformation [88], is feasible at high pH [89], but was not confirmed.

Subsequently, mineralogy controls Na release, early-hydration kinetics and sulfate demand in COCBR blended cements (Fig. 6 and Fig. A15). In sodalite-type zeolites, including cancrinite [55], ion exchange occurs through six-membered rings with apertures of 1.8–2.4 Å [90]. Thermal activation reduces this aperture and decreases the ion-exchange capacity of OH-sodalites [91], implying slower Na release for dehydroxylated phases in COCB compared to OH-sodalites in untreated BR [92]. QXRD shows that co-calcination (BR to COCB) decreases cancrinite content and reduces its d_{110} spacing, indicating a distortion of the zeolitic framework (Fig. S 8) [90]. Across the COCBR series early hydration kinetics vary (Fig. 4 (c)), mainly due to DSP mineralogy and content, because overall reactivity [8], SSA and kaolinite source were kept constant [20].

In VBR systems, Na is partly retained in residual SCM. Its release appears to depend on the slower dissolution of the VBRs alumosilicate glass (Fig. 6, Fig. 9). This behavior coincided with less accelerated AFm precipitation (Fig. 3) and slower strength development (Fig. 2 (b)). At later ages and high replacement levels the higher Ca content and slower Na release of VBR (Table 1, Fig. A14) are consistent with increased hydrate precipitation and improved late-age performance. Time-resolved pore solution and phase assemblage data during the first 24 h of hydration are required to resolve the mechanisms behind the accelerated AFm precipitation. Thermodynamic and kinetic descriptions of the modified BR's reactive contribution require targeted dissolution experiments similar to [93]. Such data would support quantitative hydration-modeling and the optimization of modified BR blended cements.

4.3. Modified BRs and their influence on hydrate phases

This section discusses the impact of modified BRs on C-A-S-H and AFm composition and examines the differences between thermodynamic modeling results and 180 d phase assemblages.

4.3.1. Composition of C-A-S-H phases

C-A-S-H remains the dominant hydrate in most BR blended systems, but its composition changed at 30–50 wt% substitution. Across untreated, co-calcined and vitrified BR blends, C-A-S-H remains Ca-rich (Ca/Si 1.8–2.0, comparable to OPC, Table 4). No causal relationship between Na content and Ca/Si ratio was observed, consistent with Kumar et al. [94]. Al/Si ratios increased to 0.3–0.4, comparable to metakaolin-rich LC^3–50 binders [70]. The alkali content of C-A-S-H increased with the Al/Si ratio, consistent with [95,96]. Although high Ca/Si was reported to suppress alkali uptake by C-A-S-H [96], this trend is not evident in Table 4.

Fe-rich modified BRs increased Fe contents in C-A-S-H regions (Table 4), suggesting either intergrowth with nanocrystalline ferrihydrite or structural incorporation of Fe into C-A-S-H. After 365 d traces of Fe/Si-hydrogarnets were detected by XRD in the most iron-rich systems (VBR-50, COCBR-50). Intergrowth of ferrihydrite and C-A-S-H, followed by the formation of Fe/Si-hydrogarnet, was reported for copper slag-blended cement [97]. A similar process may occur in modified BR blends.

Siramanont systematically studied Fe (III) inclusion in synthetic C-A-S-H [98] and reported X-ray amorphous Fe phases and Fe-hydrogarnets, accompanied by structural changes in C-A-S-H, over a wide Fe (III) concentration range. Fe (III) partially occupied Ca^{2+} positions in the C-A-S-H interlayer [99,100]. Mancini et al. reported Fe (II) surface sorption and uptake in the C-A-S-H interlayer [101], which might be relevant for VBR systems. Siramanont observed greater Fe uptake at higher Ca/Si ratios, while Mancini [101] found no trends between Ca/Si ratio and Fe (II) uptake. The highest reported Fe content of 16 wt% (Fe/Si ≈ 0.45) [100] is comparable to the highest ratio measured here (VBR-30, Table 4).

4.3.2. Composition of AFm phases

AFm contents in modified BR blends are comparable to those of metakaolin-rich LC^3 systems [70,102]. However, AFm phases in BR-blended cements contain up to 5 times more alkalis than FA-30 (Table 4). QXRD and TGA provide no evidence for U-phase precipitation [66].

Strätlingite was only detected in the CH depleted SL-30 blend, consistent with thermodynamic modeling (Table 5) and previous observations in metakaolin-rich LC^3 binders [102] and OPC-CSA blends [103]. The Ca/Al ratios of AFm phases in COCBR, BR and VBR blended cements match those of sulfate/carbonate AFms (Table 4). The AFms in COCBR and VBR blend show substantial Fe substitution (Table 4), consistent with Dilnesa et al. [104,105] and Lechevallier et al. [106], who showed that Fe-bearing monosulfate, hemi- and monocarbonate can form in cementitious systems at high Fe activities.

In cement pastes, sulfate- and carbonate-AFm phases commonly form solid-solutions, mainly OH^-/SO_4^{2-} and SO_4^{2-}/CO_3^{2-}, with variable water contents [28,64]. This broadens diffraction peaks and complicates the comparison between paste-derived and synthetic AFm. Fe-bearing AFm phases generally show stronger peak broadening than Fe-free AFm [106]. Fig. 12 compares diffractogram excerpts of COCB-30,

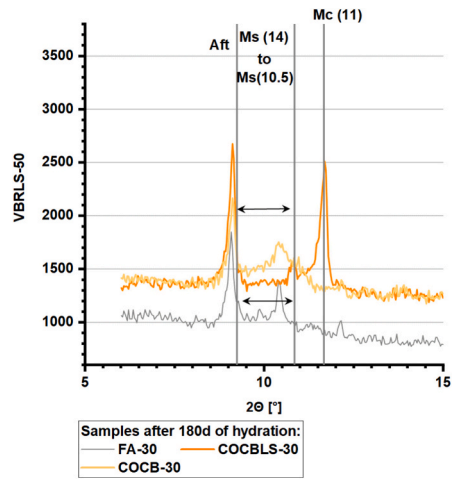


Fig. 12. Excerpt of X-ray diffractograms highlighting the shift of the AFm (001) basal reflection in modified BR blended cements.

COCBLS-30 and FA-30 after 180 d to illustrate the observed differences in AFm peak shape.

In FA-30, the AFm basal reflection falls within the range reported for partially carbonated monosulfate in FA-blended cements [28]. Although the FA contained less than 1 wt% of calcite, carbonation during sample preparation cannot be excluded. In COCB-30, the AFm basal reflection was broad and overlapped the range of monosulfate-, carbonate- and chloride-AFm phases [28]. A similar behavior is observed for COCA and COCC blends. The broad reflections may result from the coexistence of Fe- and Al-monosulfate [105] and variations of the interlayer composition involving Na or transition metals [66,85]. VBR-30 showed a slimmer monosulfate 14 (001) reflection (full width at half maximum ≈ 1° 2Θ). These differences between COCB and VBR systems require further investigation.

Limestone addition always promoted the precipitation of Fe-rich hemi- and monocarbonate with less variable basal spacing, as shown for COCBLS-30 (Fig. 12).

Mixed Al-/Fe-monocarbonate solid solutions were reported during brownmillerite hydration [106], but their stability and formation in Fe-rich blended cements requires further investigation.

Chromium (Cr) is among most critical elements for the environmental compatibility of BR blended cements [8] and its immobilization in AFm phases may help to explain the promising leaching performance reported for COCBR blended cements [21]. The incorporation of $Cr_2O_6^{2-}$ and Cr^{3+} ions into AFt and AFm structures was reported [85]. However, the formation and stability of Cr-bearing aluminate hydrates at the elevated pH of BR blended cements remains unresolved. Environmental assessments should focus on total heavy-metal contents and the determination of release rates conducted under relevant exposure conditions. Evaluating these results against regulatory limits is crucial for evaluating the applicability of modified BRs as alternative SCMs.

Compared with FA blended cements, modified BR blends formed less pozzolanic C-A-S-H but more aluminate hydrates. AFm precipitation was accelerated during early hydration and reached contents up to 20 g/$100g_{paste}$. AFm precipitation within the pore space may contribute substantially to pore refinement and strength development. A similar contribution of AFm to late-age strength was reported for LC^3 binders [47,107]. In BR and COCBR blends accelerated AFm precipitation increased 2 d strength, while AFm represents a substantial fraction of the late age phase assemblage in all modified BR blends.

Zunino et al. showed that increased Al activity in pore solution is a key driver of AFm precipitation in aluminate rich blended cements [108]. Although they increased Al and Fe concentrations using ethanolamine and not pH, they also observed increased and accelerated AFm precipitation without a loss of AFt or C-A-S-H formation. Their work on activated LC^3 binders links enhanced AFm precipitation to pore refinement and strength development in Al-rich blended cements [108] and is consistent with our findings.

4.4. Towards the application of BR-blended cements

High BR incorporation in cement generally requires thermochemical activation or blending with reactive SCMs [109,110]. Among the routes investigated, co-calcination and vitrification provided the most favourable performance at 30 wt% substitution while retaining a C-A-S-H dominated hydrate assemblage. The enhanced formation of aluminate hydrates also ensured clear benefits from ternary formulations including limestone, which promote carboaluminate formation and enhance mechanical performance (Section 3.1). The distinct advantages of both activation routes are discussed below.

Vitrification completely transforms the feedstocks mineralogy but requires notable amounts of Ca and Si bearing additives and high temperatures (1250 °C) [21]. The resulting VBR can be adjusted through feed chemistry, which simplifies quality assurance and enables the production of a predictable SCM from diverse raw materials [21]. Life-cycle assessments by Gregoriades et al. indicate that VBR can reduce the carbon footprint of blended cements despite the energy intensive process [111]. During hydration VBR behaves similar to alkali-rich GGBFS, providing good workability and slag-cement like phase assemblage and morphology [112]. Among the studied systems VBRLS-30 (55 wt% clinker content) is closest to application. If standardized as a new SCM, VBRLS-30 blends would fit within the CEM II-C category, assuming the sulfate limit for slag cements is applied [3].

Co-calcination is the least energy-intensive activation route, because it avoids melting and operates at 750 to 800 °C. This reduces equipment demands and makes the process economically and environmentally comparable to clay calcination. However, stable performance requires continuous monitoring of clay and BR mineralogy to adjust feed composition and maintain constant SCM reactivity (Section 3.2.1. and [20]). DSP composition and content fluctuate between plants [9] and during the operation of individual alumina plants [113]. If defined as a new SCM type, COCBLS-30 could also qualify for standardization within the CEM II-C category and represents the most deployment-ready BR-derived binder investigated in this study.

Reductively smelted BR (SL) is an Al-rich, highly reactive material generated during ferrotitanium production [39]. Although this route upcycles mineral waste its environmental impact requires critical assessment because processing occurs above 1500 °C [22]. At 30 wt% replacement, SL caused rapid CH depletion and produced a hydrate assemblage dominated by AFm and strätlingite. Its high Al availability may be beneficial for super-sulfated cements or other AFt based binder concepts. If a C-A-S-H dominated microstructures is required, SL could be combined with Si-rich pozzolans or inert fillers in ternary or quaternary binders. Further hydration studies are required to optimize phase assemblages and identify viable binder formulations.

Low-clinker cements (<50 wt% clinker) could maximize BR valorisation. In this range, VBR and COCBR blends are promising, although sulfate balance and mix design need further optimization. The SLIM test [53] can support this optimization by classifying the SCMs reactivity and its effects on sulfate demand. The modified BR blends showed some tolerance against undersulfation (Section 3.2.1). However, the required sulfate contents to optimize aluminate reactions may exceed the limits of EN 197-1.

Further microstructural studies should characterize the changes in AFm and C-A-S-H structure and identify the most performant hydrate

assemblages. The present results indicate a shift in hydrate assemblage with decreasing clinker content: AFt and AFm become major hydrates, whereas C-A-S-H precipitation decreases. At 50 wt% COCBR or VBR substitution Fe-hydrogarnet formation becomes evident. Ca-rich modified BRs (VBR and SL) may be better suited for high substitution levels, as demonstrated for the VBRLS-50 system.

VBRLS-50 was the most promising system in this study. Strong VBR-limestone synergies increased the SCMs reactive contribution through nucleation effects, carboaluminate precipitation and subsequent AFt stabilization. VBRLS-50 develops a slag-cement-like microstructure dominated by C-A-S-H, AFt, carbonate AFm and portlandite [58]. It retained good workability and achieved higher early- and late-age strengths than the corresponding binary system (VBR-50). Further optimization of binder composition, sulfate balance and SCM fineness is required to fully exploit its potential.

Progress towards the standardization of these systems requires a systematic assessment of engineering, durability, and environmental compatibility following NPR-CEN/TR 16912 [114].

5. Conclusions

This study provides the first quantitative comparison of untreated, co-calcined, vitrified and reductively smelted bauxite residues (BRs) as SCMs, benchmarked against OPC and fly-ash blended cement. The combined phase-assemblage and pore-solution dataset convers substitution levels of 10 to 50 wt% and identifies promising pathways for using high volumes of BR in blended cements.

Most modified BR blended cements show alkali-induced acceleration of hydration and pozzolanic reactions. This effect is primarily controlled by the SCMs Na-release rate, which depends more on the mineralogy of the Na-bearing phases than on Na content. The Consumption of zeolitic phases of the BRs desilication product indicated their reactivity, consistent with thermodynamic predictions for the pozzolanic reaction of OH-sodalites [8]. Dissolution of modified BRs during the first 48 h impacts early hydration kinetics, setting behavior, and strength development. Rapid AFm formation should contribute to the early-age performance of modified BR blended cements.

At 30 wt% co-calcined and vitrified BR addition clinker DoH and strength development evolved more similar to OPC than FA blended systems, resulting in near-constant phase assemblages between 56 and 90 d. At 30–50 wt% substitution these binders are dominated by C-A-S-H, substantial AFm and AFt contents and residual portlandite. At 50 wt% replacement traces of Fe/Si-hydrogarnets appear after 365 d. Limestone addition improves early and late age strength, by promoting carboaluminate AFm formation while maintaining AFt. The elevated Na and Fe contents of AFm and C-A-S-H phases require further investigation. Reductively smelted BR is highly reactive. It depletes portlandite at 30 wt% replacement leading to a monosulfate and strätlingite dominated microstructure.

This study identifies several co-calcined and vitrified BR blended cements with potential for industrial adaptation. Ternary blends of 30 wt% co-calcined or vitrified BR and limestone are closest to the compositional requirements of EN 197-1. Co-calcined BR blends show rapid strength development, which makes them suitable for time-critical applications. Vitrified BR/limestone systems are particularly promising low-carbon binders, enabling clinker replacement levels of up to 65 wt %.

Finally, the durability and environmental compatibility of the modified BR-blended cements must be assessed at the concrete scale to identify suitable applications and support the development of competitive, sustainable concretes.

CRediT authorship contribution statement

Michael Wenzel: Writing – review & editing, Writing – original draft, Visualization, Methodology, Investigation, Formal analysis, Data curation, Conceptualization. **Fabien Georget:** Writing – review & editing, Validation, Supervision, Project administration. **Thomas Matschei:** Writing – review & editing, Validation, Supervision, Funding acquisition.

Declaration of Generative AI and AI-assisted technologies in the writing process

AI tools (ChatGPT 5.0, OpenAI) were used to improve the reader's experience. The writing process was structured as follows:

1.) A full text was written by the authors.
2.) Several loops of paragraph by paragraph optimization using AI and manual adjustment of the AI results were carried out to shorten the manuscript and refine the phrasing.
3.) The manuscript was manually rephrased on a sentence-by-sentence approach to ensure the quality of the content and properly emphasize core messages.

AI tools were not used to process data, curate literature, or restructure this manuscript.

Declaration of competing interest

The authors declare the following financial interests/personal relationships which may be considered as potential competing interests: Michael Wenzel reports financial support was provided by German Research Foundation (SFB TRR 280 Project ID 417002380). Michael Wenzel reports financial support was provided by European Union (Horizon 2020 Grant Agreement No. 958208). This manuscript was written in the context of the ReActiv project. In this project several acknowledged project partners (VITO, KU-Leuven) have been filing patents for the activation technologies. The authors want to stress that only the analysis and the results of the hydration study and not the SCM development are part of their intellectual property. If there are other authors, they declare that they have no known competing financial interests or personal relationships that could have appeared to influence the work reported in this paper.

Acknowledgements

This work was funded by the EU Horizon 2020 program (Grant No. 958208) and the Deutsche Forschungsgemeinschaft (DFG, German Research Foundation) SFB/TRR 280 Project-ID: 417002380. The authors thank the ReActiv partners for (Holcim Innovation Center, KU-Leuven, VITO and NTUA) providing the materials used in this study. We especially thank Michiel Giels (KUL), Tobias Hertel (KUL), Natalia Pires-Martins (VITO), Arne Peys (VITO), Elsa Qoku (RWTH) and Ken Evans (IAI) for their valuable scientific input, experimental support and characterization data. We thank Gabriel Pham, Phillipe Bernard (both Holcim innovation centre) for the material supply and Annika Blum (TU Clausthal) for Raman measurements.

Appendix A

Table A6
List of abbreviations, grouped according to the main sections of the manuscript.

Abbreviation	Meaning
AFm	Ca-Al layered hydroxides
AFt	ettringite
ATR-FTIR	Attenuated Total Reflection - Fourier Transformed Infrared Spectroscopy
BR	Bauxite Residue (B)
BSE	Backscattered Electron Image
C-A-S-H	calcium aluminosilicate hydrate
C-S-H	calcium silicate hydrate
CH	Portlandite
COCA	co-calcined Bauxite Residue A
COCB	co-calcined Bauxite Residue B
COCC	co-calcined Bauxite Residue C
COCBRs	co-calcined Bauxite Residues (all of them)
DSP	Desilication Product
FA	Siliceous Fly Ash
GGBFS	Ground Granulated Blast Furnace Slag
HDPE	High Density Polyethylene
ICP-OES	Induced Plasma Coupled Optical Emission Spectroscopy
IC	Ion Chromatography
LS	Limestone
LoI	Loss on ignition
N-A-S-H	Sodium Aluminosilicate Hydrate
OPC	Ordinary Portland Cement (CEM I)
PSD	Particle Size Distribution
QXRD	Quantitative X-ray Diffraction
RAMAN	Raman Spectroscopy
R_{CH}	Normalized Portlandite Content
R^3 test	Rapid Relevant and Reliable test for pozzolanic reactivity
SAI	Strength Activity Index
ScDT	Sulfate Carrier Depletion Time
SCM	Supplementary Cementitious Material
SDT	Sulfate Depletion Time
SEM-EDX	Scanning Electron Microscopy - Energy dispersive X-ray Spectroscopy
SI	Saturation Index
SL	Reductively Smelted Bauxite Residue 2
SLiM test	Sulfate Limited Model System test for early age reactivity of calcined clays
SSA	Specific Surface Area
TGA	Thermogravimetry Analysis
VBR	vitrified Bauxite Residue B
w/b	Water to Binder ratio
XRD	X-ray Diffraction
XRF	X-ray Fluorescence Spectroscopy

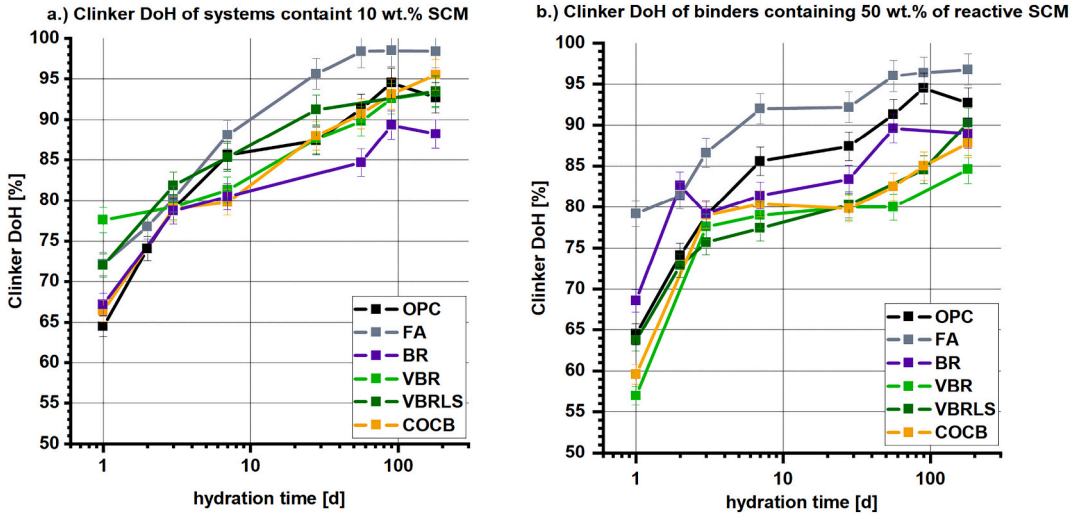


Fig. A13. (a) DoH evolution of 10 wt% SCM blended cements and (b) of 50 wt% SCM blended cements.

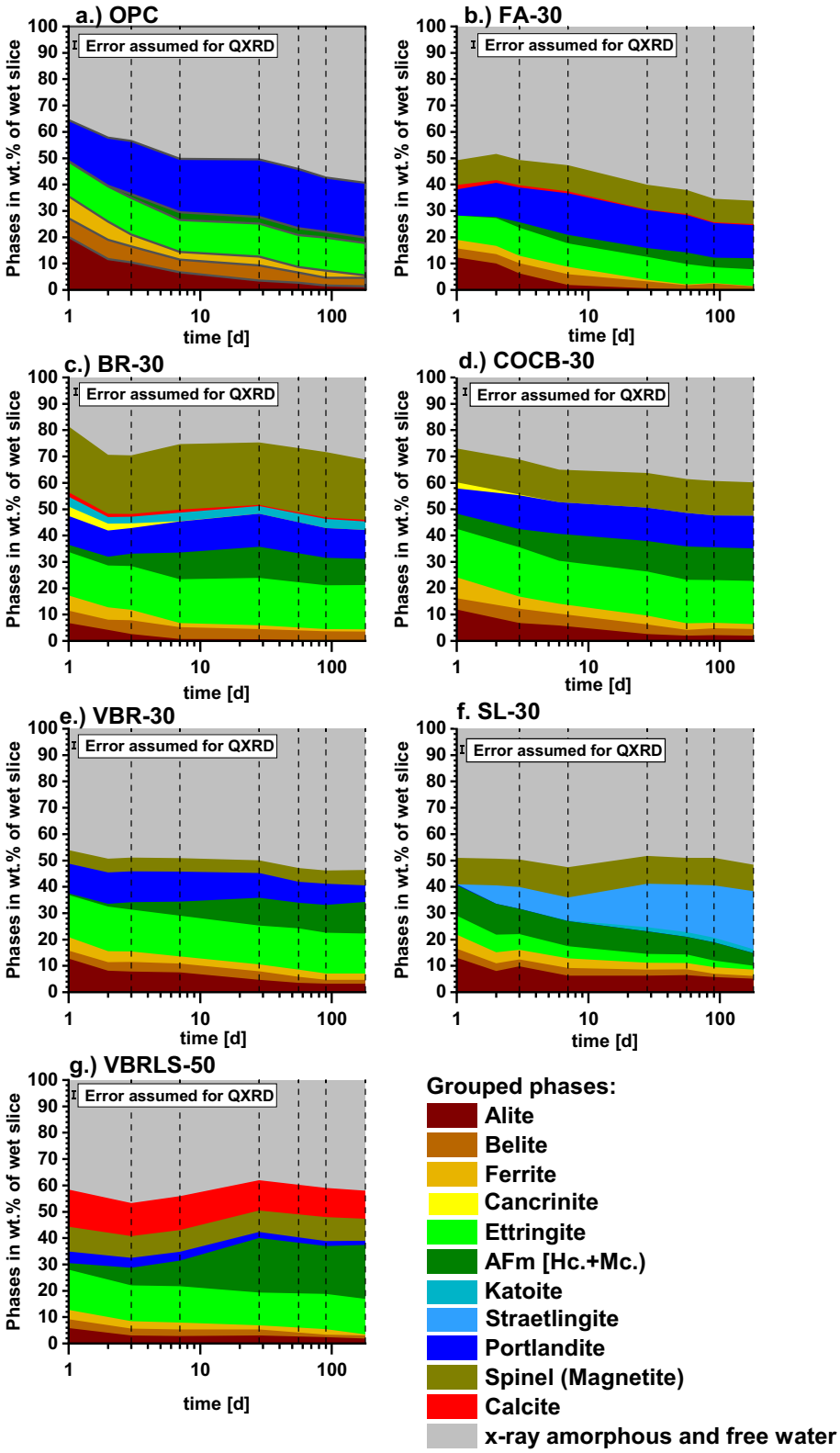


Fig. A14. Evolution of phase assemblage of selected systems, comparison of the differently treated BRs (a–f), and the lowest clinker system (VBRLS-50) investigated in this study (g).

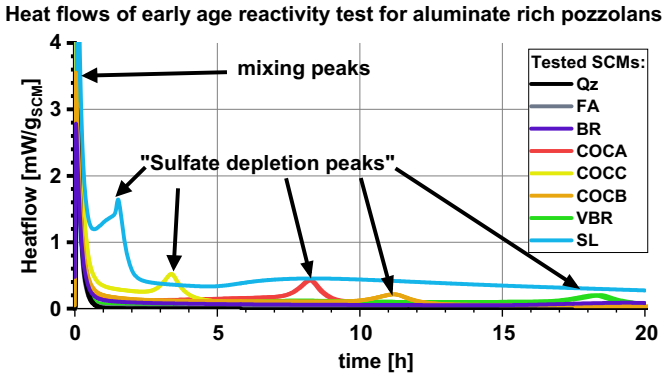


Fig. A15. Heat flow curves during the SLiM test.

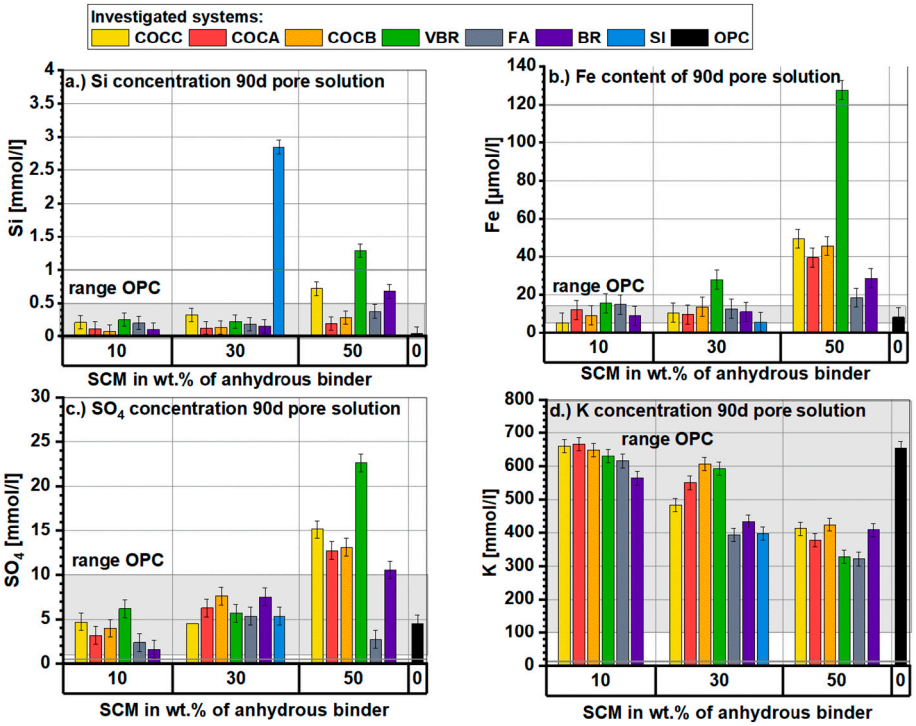


Fig. A16. Pore solution composition after 90d of hydration (a) $Si^{2}+$ concentrations, (b) $Fe^{2+/3+}$ concentration, (c) sulfate concentration and (d) K^{+} concentration. The grey areas symbolize the range of OPC values reported by [72].

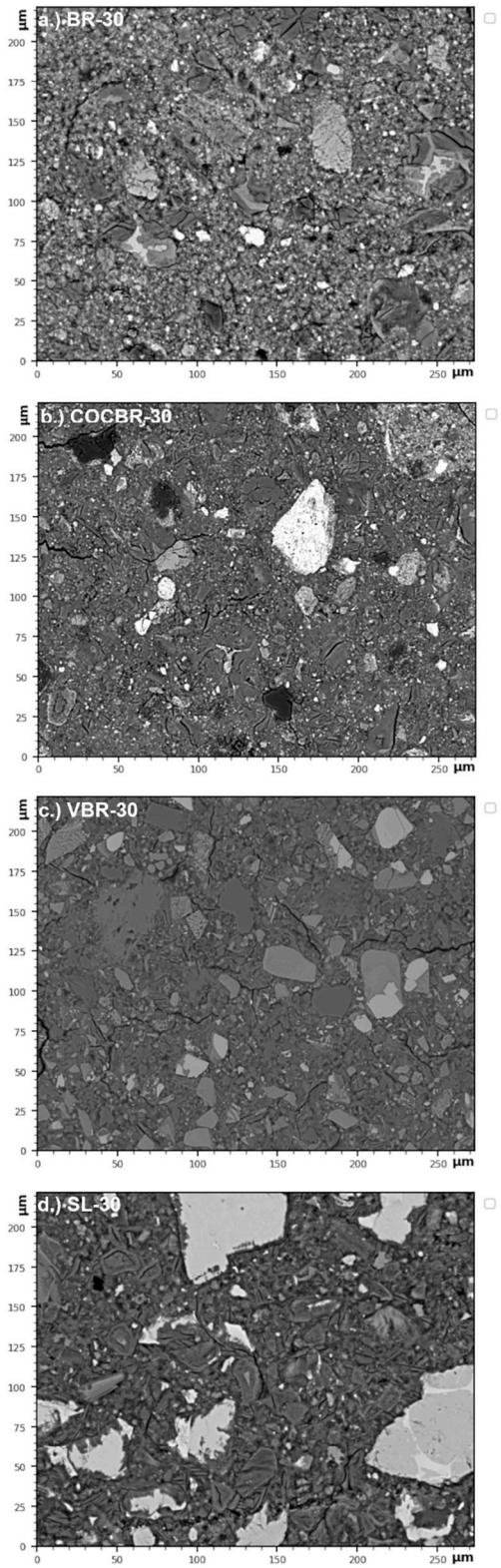


Fig. A17. BSE micrographs of the investigated SEM-EDX samples; (a) BR-30, (b) COCB-30, (c) VBR-30 and (d) SL-30.

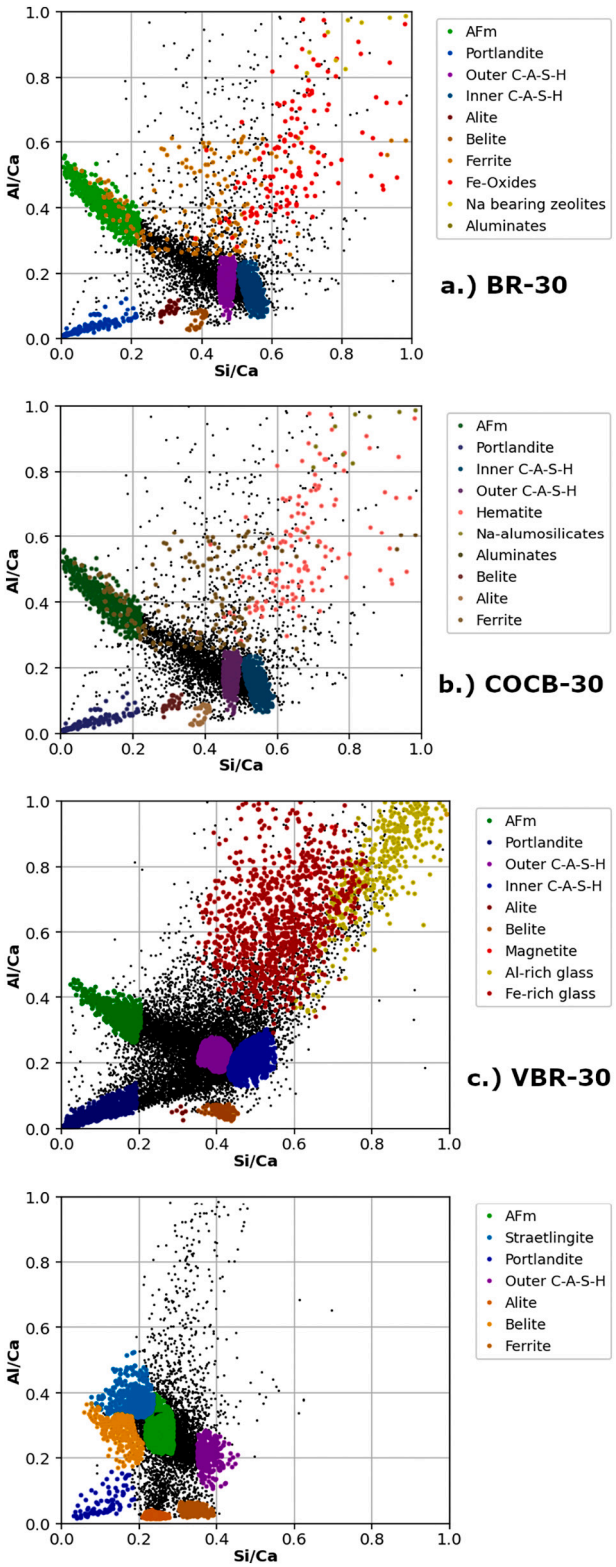


Fig. A18. Al/Ca versus Si/Ca ratio plots of (a) BR-30, (b) COCB-30, (c) VBR-30 and (d) SL-30.

Appendix B. Supplementary data

Supplementary data to this article can be found online at https://doi.org/10.1016/j.cemconres.2026.108384.

Data availability

The data used for this publication have been included in the supplementary files are published in a separate supplementary file.

References

[1] Cembuerau, Cementing the European Green Deal – Reaching Climate Neutrality Along the Cement and Concrete Value Chain by 2050, Cembuerau the European Cement Association, Brussels, 2020 assessed 03.03.2025, https://cembureau.eu/library.

[2] Global Cement and Concrete Association, Concrete Future - The GCCA 2050 Cement and Concrete Industry Roadmap for Net Zero Concrete, Global Cement and Concrete Association, London, 2025. https://globalabc.org/index.php/resources/publications/gcca-2050-cement-and-concrete-industry-roadmap-net-zero-concrete (accessed March 18, 2025).

[3] Cement - Part 1: Composition, Specifications and Conformity Criteria for Common Cements, 2011, https://doi.org/10.31030/1758792.

[4] Y. Dhandapani, S. Joseph, S. Bishnoi, W. Kunther, F. Kanavaris, T. Kim, E. Irassar, A. Castel, F. Zunino, A. Machner, Durability performance of binary and ternary blended cementitious systems with calcined clay: a RILEM TC 282-CCL, review, Mater. Struct. 55 (2022) 145, https://doi.org/10.1617/s11527-022-01974-0.

[5] M. Hossain, M. Karim, M. Hasan, M. Hossain, M. Zain, Durability of mortar and concrete made up of pozzolans as a partial replacement of cement: a review, Construct. Build. Mater. 116 (2016) 128–140, https://doi.org/10.1016/j.conbuildmat.2016.04.147.

[6] A. Peys, V. Isteri, J. Yliniemi, A.S. Yorkshire, P.N. Lemougna, C. Utton, J. L. Provis, R. Snellings, T. Hanein, Sustainable iron-rich cements: raw material sources and binder types, Cem. Concr. Res. 157 (2022) 106834, https://doi.org/10.1016/j.cemconres.2022.106834.

[7] R. Snellings, P. Suraneni, J. Skibsted, Future and emerging supplementary cementitious materials, Cem. Concr. Res. 171 (2023) 107199, https://doi.org/10.1016/j.cemconres.2023.107199.

[8] M. Wenzel, F. Georget, T. Matschei, From bauxite residue mineralogy to reactivity and properties of blended cements, Cem. Concr. Res. 192 (2025) 107854, https://doi.org/10.1016/j.cemconres.2025.107854.

[9] M. Gräfe, G. Power, C. Klauber, Bauxite residue issues: III. Alkalinity and associated chemistry, Hydrometallurgy 108 (2011) 60–79, https://doi.org/10.1016/j.hydromet.2011.02.004.

[10] A. Goronovski, R.M. Rivera, T. Van Gerven, A.H. Tkaczyk, Radiological assessment of bauxite residue processing to enable zero-waste valorisation and regulatory compliance, J. Clean. Prod. 294 (2021) 125165, https://doi.org/10.1016/j.jclepro.2020.125165.

[11] A. Ruys, 3 - refining of alumina: the Bayer process, in: A. Ruys (Ed.), Alumina Ceramics, Woodhead Publishing, 2019, pp. 49–70. https://www.sciencedirect.com/science/article/pii/B9780081024423000038.

[12] L. Huang, P. Yan, Effect of alkali content in cement on its hydration kinetics and mechanical properties, Construct. Build. Mater. 228 (2019) 116833, https://doi.org/10.1016/j.conbuildmat.2019.116833.

[13] D.P. Bentz, Influence of alkalis on porosity percolation in hydrating cement pastes, Cem. Concr. Compos. 28 (2006) 427–431, https://doi.org/10.1016/j.cemconcomp.2006.01.003.

[14] F.R. Feret, Selected applications of Rietveld-XRD analysis for raw materials of the aluminum industry, Powder Diffract. 28 (2013) 112–123, https://doi.org/10.1017/S088571561300016X.

[15] X. Pan, H. Wu, H. Yu, S. Bi, Precipitation of desilication products in CaO-Na2O-Al2O3-SiO2-H2O system based on the Bayer process, Hydrometallurgy 197 (2020) 105469, https://doi.org/10.1016/j.hydromet.2020.105469.

[16] L. Senff, R.C.E. Modolo, A.S. Silva, V.M. Ferreira, D. Hotza, J.A. Labrincha, Influence of red mud addition on rheological behavior and hardened properties of mortars, Construct. Build. Mater. 65 (2014) 84–91, https://doi.org/10.1016/j.conbuildmat.2014.04.104.

[17] D.V. Ribeiro, J.A. Labrincha, M.R. Morelli, Potential use of natural red mud as pozzolan for Portland cement, Mater. Res. 14 (2011) 60–66, https://doi.org/10.1590/S1516-14392011005000001.

[18] J. Pera, R. Boumaza, J. Ambroise, Development of a pozzolanic pigment from red mud, Cem. Concr. Res. 27 (1997) 1513–1522, https://doi.org/10.1016/S0008-8846(97)00162-2.

[19] M. Giels, T. Hertel, T.N. Nguyen, Y. Pontikes, Bringing metallurgy and cement industry closer: Fe-rich glass as a supplementary cementitious material, J. Sustain. Metall. (2025), https://doi.org/10.1007/s40831-025-01129-9.

[20] A. Peys, T. Hertel, R. Snellings, Co-calcination of bauxite residue with kaolinite in pursuit of a robust and high-quality supplementary cementitious material, Front. Mater. 9 (2022) 384, https://doi.org/10.3389/fmats.2022.913151.

[21] T. Hertel, A. Van den Bulck, B. Blanpain, Y. Pontikes, Correlating the amorphous phase structure of vitrified bauxite residue (red mud) to the initial reactivity in binder systems, Cem. Concr. Compos. 127 (2022) 104410, https://doi.org/10.1016/j.cemconcomp.2022.104410.

[22] D. Sparis, A. Lazou, E. Balomenos, D. Panias, Thermodynamics of aluminothermic processes for ferrotitanium alloy production from bauxite residue and ilmenite, Metals 14 (2024) 200–215, https://doi.org/10.3390/met14020200.

[23] D. Londono-Zuluaga, A. Gholizadeh-Vayghan, F. Winnefeld, F. Avet, M. Ben Haha, S.A. Bernal, Ö. Cizer, M. Cyr, S. Dolenec, P. Durdzinski, J. Haufe, D. Hooton, S. Kamali-Bernard, X. Li, A.T.M. Marsh, M. Marroccoli, M. Mrak, Y. Muy, C. Patapy, M. Pedersen, S. Sabio, S. Schulze, R. Snellings, A. Telesca, A. Vollpracht, G. Ye, S. Zhang, K.L. Scrivener, Report of RILEM TC 267-TRM phase 3: validation of the R3 reactivity test across a wide range of materials, Mater. Struct. 55 (2022) 142, https://doi.org/10.1617/s11527-022-01947-3.

[24] T.R. Muzenda, F. Georget, T. Matschei, Early Reactivity Assessment of Calcined Clays and the Impact of Secondary Phases, Special Publication 362, 2024, pp. 720–732, https://doi.org/10.14359/51742004.

[25] S. G., C.L. Yannick Demeusy, Rheology and Early-Age Reactivity of Calcined Kaolinite, ACI Symposium Publication 362, 2024, https://doi.org/10.14359/51741015.

[26] J.H. Hubbell, S.M. Seltzer, Tables of X-Ray MAss Attenuation Coefficients and Mass Energy-Absorption Coefficients, 1996, https://doi.org/10.18434/T4D01F.

[27] B. Lothenbach, P. Durdzinski, K. de Weerdt, Chapter 5: thermogravimetric analysis, in: A Practical Guide to Microstructural Analysis of Cementitious Materials, CRC Press Taylor & Francis Group, New York, 2016, pp. 178–206.

[28] F. Georget, B. Lothenbach, W. Wilson, F. Zunino, K.L. Scrivener, Stability of hemicarbonate under cement paste-like conditions, Cem. Concr. Res. 153 (2022) 106692, https://doi.org/10.1016/j.cemconres.2021.106692.

[29] C. Beaumont, A. Goodman, P. Greenfield, Hackable user interfaces in astronomy with glue, in: Astronomical Data Analysis Software and Systems XXIV (ADASS XXIV), 2015, p. 101. https://aspbooks.org/custom/publications/paper/495-0101.html.

[30] T. Robitaille, C. Beaumont, P. Qian, M. Borkin, A. Goodman, glueviz v0. 15.2: multidimensional data exploration, in: Scientific Python Packages and Papers, 2019, https://doi.org/10.5281/zenodo.774845.

[31] F. Georget, W. Wilson, K.L. Scrivener, edxia: microstructure characterisation from quantified SEM-EDS hypermaps, Cem. Concr. Res. 141 (2021) 106327, https://doi.org/10.1016/j.cemconres.2020.106327.

[32] T. Thoenen, W. Hummel, U. Berner, E. Curti, The PSI/Nagra Chemical Thermodynamic Database 12/07, Nuclear Energy and Safety Research Department Laboratory for Waste Management (LES), Pauls Scherrer Institut, Villingen, 2014. https://www.dora.lib4ri.ch/psi/dload/psi%3A29731/PDF/Thoenen-2014-The_PSI-Nagra_chemical_thermodynamic_database_12-07-(published_version).pdf.

[33] B. Lothenbach, D.A. Kulik, T. Matschei, M. Balonis, L. Baquerizo, B. Dilnesa, G. D. Miron, R.J. Myers, Cemdata18: a chemical thermodynamic database for hydrated Portland cements and alkali-activated materials, Cem. Concr. Res. 115 (2019) 472–506, https://doi.org/10.1016/j.cemconres.2018.04.018.

[34] G. Dan Miron, O. Marinich, M. Marques Fernandes, D.A. Kulik, B. Baeyens, R. Wust, The optimized gems Claysor model and data bases to support Nagra safety assessments for deep geological repository, in: Nantes, 2023, pp. 517–518. https://inis.iaea.org/records/takmf-wav94.

[35] B. Ma, B. Lothenbach, Synthesis, characterization, and thermodynamic study of selected K-based zeolites, Cem. Concr. Res. 148 (2021) 106537, https://doi.org/10.1016/j.cemconres.2021.106537.

[36] B. Ma, B. Lothenbach, Synthesis, characterization, and thermodynamic study of selected Na-based zeolites, Cem. Concr. Res. 135 (2020) 106111, https://doi.org/10.1016/j.cemconres.2020.106111.

[37] B. Ma, B. Lothenbach, Thermodynamic study of cement/rock interactions using experimentally generated solubility data of zeolites, Cem. Concr. Res. 135 (2020) 106149, https://doi.org/10.1016/j.cemconres.2020.106149.

[38] H.C. Helgeson, D.H. Kirkham, Theoretical prediction of the thermodynamic behavior of aqueous electrolytes at high pressures and temperatures; II, Debye-Huckel parameters for activity coefficients and relative partial molal properties, Am. J. Sci. (1981) 1249–1516. https://ajsonline.org/article/60143.pdf.

[39] D. Sparis, A. Lazou, E. Balomenos, D. Panias, BR06-Ferrotitanium Production from BR: A Study of the Aluminothermic Process, TRAVAUX 52, Proceedings of the 41st International ICSOBA Conference, Dubai, 2023, pp. 883–889, https://icsoba.org/proceedings/41st-conference-and-exhibition-icsoba-2023/?scroll_to=docs&query=Ferrotitanium+Production+from+BR (accessed February 7, 2025).

[40] M. Giels, Y. Pontikes, Novel Sustainable Binders incorporating High Volumes of Bauxite Residue, PhD Thesis, Katholieke Universiteit Leuven, Sustainable Materials Processing and Recycling (SeMPeR), 2023, https://kuleuven.limo.libis.be/discovery/search?query=any,contains,LIRIAS4079885&tab=LIRIAS&search_scope=lirias_profile&vid=32KUL_KUL:Lirias&offset=0.

[41] M. Giels, T. Hertel, K. Gijbels, W. Schroeyers, Y. Pontikes, High performance mortars from vitrified bauxite residue; the quest for the optimal chemistry and processing conditions, Cem. Concr. Res. 155 (2022) 106739, https://doi.org/10.1016/j.cemconres.2022.106739.

[42] H.F.W. Taylor, Cement Chemistry, 2nd ed, T. Telford, London, 1997.

[43] N. Roussel, C. Stefani, R. Leroy, From mini-cone test to Abrams cone test: measurement of cement-based materials yield stress using slump tests, Cem. Concr. Res. 35 (2005) 817–822, https://doi.org/10.1016/j.cemconres.2004.07.032.

[44] F. Winnefeld, A. Schöler, B. Lothenbach, Chapter 1: sample preparation, in: A Practical Guide to Microstructural Analysis of Cementitious Materials, CRC Press Taylor & Francis Group, London, n.d.: pp. 1–37.

[45] K.L. Scrivener, T. Füllmann, E. Gallucci, G. Walenta, E. Bermejo, Quantitative study of Portland cement hydration by X-ray diffraction/Rietveld analysis and independent methods, Cem. Concr. Res. 34 (2004) 1541–1547, https://doi.org/10.1016/j.cemconres.2004.04.014.

[46] B. Mota, T. Matschei, K. Scrivener, Impact of NaOH and Na2SO4 on the kinetics and microstructural development of white cement hydration, Cem. Concr. Res. 108 (2018) 172–185, https://doi.org/10.1016/j.cemconres.2018.03.017.

[47] F. Zunino, K. Scrivener, Microstructural developments of limestone calcined clay cement (LC3) pastes after long-term (3 years) hydration, Cem. Concr. Res. 153 (2022) 106693, https://doi.org/10.1016/j.cemconres.2021.106693.
[48] M.U. Okoronkwo, F.P. Glasser, Stability of strätlingite in the CASH system, Mater. Struct. 49 (2016) 4305–4318, https://doi.org/10.1617/s11527-015-0789-x.
[49] H.G. Midgley, P.B. Rao, Formation of stratlingite, 2CaO.SiO2.Al2O3.8H2O, in relation to the hydration of high alumina cement, Cem. Concr. Res. 8 (1978) 169–172, https://doi.org/10.1016/0008-8846(78)90005-4.
[50] T. Chappex, K.L. Scrivener, The influence of aluminium on the dissolution of amorphous silica and its relation to alkali silica reaction, Cem. Concr. Res. 42 (2012) 1645–1649, https://doi.org/10.1016/j.cemconres.2012.09.009.
[51] E. Berodier, K. Scrivener, Understanding the filler effect on the nucleation and growth of C-S-H, J. Am. Ceram. Soc. 97 (2014) 3764–3773, https://doi.org/10.1111/jace.13177.
[52] Y. Demeusy, T.R. Muzenda, A.-C. Guillet, S. Gauffinet, F. Georget, T. Matschei, C. Labbez, Early-Reactivity of Calcined Clays and its Impact on Fresh Cement Paste Rheology, Available at SSRN 5364143 (n.d.).
[53] T.R. Muzenda, Y. Demeusy, F. Georget, C. Labbez, T. Matschei, Sulfate adjustment and early reactivity in cements containing kaolinitic calcined clays: investigation and assessment via a sulfate-limited model system, Cem. Concr. Res. 199 (2026) 108060, https://doi.org/10.1016/j.cemconres.2025.108060.
[54] H. Peng, J. Vaughan, Aluminate effect on desilication product phase transformation, J. Cryst. Growth 492 (2018) 84–91, https://doi.org/10.1016/j.jcrysgro.2018.04.013.
[55] B. Xu, P. Smith, C. Wingate, L. De Silva, The effect of calcium and temperature on the transformation of sodalite to cancrinite in Bayer digestion, Hydrometallurgy 105 (2010) 75–81, https://doi.org/10.1016/j.hydromet.2010.07.010.
[56] Y. Deng, M. Flury, J.B. Harsh, A.R. Felmy, O. Qafoku, Cancrinite and sodalite formation in the presence of cesium, potassium, magnesium, calcium and strontium in Hanford tank waste simulants, Appl. Geochem. 21 (2006) 2049–2063, https://doi.org/10.1016/j.apgeochem.2006.06.019.
[57] S. Hsu, M. Chi, R. Huang, Effect of fineness and replacement ratio of ground fly ash on properties of blended cement mortar, Construct. Build. Mater. 176 (2018) 250–258, https://doi.org/10.1016/j.conbuildmat.2018.05.060.
[58] O.R. Ogirigbo, L. Black, Influence of slag composition and temperature on the hydration and microstructure of slag blended cements, Construct. Build. Mater. 126 (2016) 496–507, https://doi.org/10.1016/j.conbuildmat.2016.09.057.
[59] I. Pane, W. Hansen, Investigation of blended cement hydration by isothermal calorimetry and thermal analysis, Cem. Concr. Res. 35 (2005) 1155–1164, https://doi.org/10.1016/j.cemconres.2004.10.027.
[60] T.C. Powers, T.L. Brownyard, Studies of the physical properties of hardened Portland cement paste, in: International Concrete Abstracts Portal, Research Laboratories of the Portland Cement Association, 1948, pp. 669–712, https://doi.org/10.14359/15304.
[61] K. Evans, The history, challenges, and new developments in the management and use of bauxite residue, J. Sustain. Metall. 2 (2016) 316–331, https://doi.org/10.1007/s40831-016-0060-x.
[62] G.N. Angelopoulos, M. Georgiou, P. Oustadakis, Preliminary Characterization of Three Metallurgical Bauxite Residue Samples, 2021, p. 66, https://doi.org/10.3390/materproc2021005066.
[63] Y. Yu, G. Guoqing, Quantification of GGBS hydration using deep learning - a comparison with SEM-EDX mapping, PONKCS XRD and isothermal calorimetry methods, Cem. Concr. Res. 197 (2025), https://doi.org/10.1016/j.cemconres.2025.107960.
[64] T. Matschei, B. Lothenbach, F. Glasser, The AFm phase in Portland cement, Cem. Concr. Res. 37 (2007) 118–130, https://doi.org/10.1016/j.cemconres.2006.10.010.
[65] R. Rinaldi, M. Sacerdoti, E. Passaglia, Strätlingite: crystal structure, chemistry, and a reexamination of its polytpye vertumnite, Eur. J. Mineral. 2 (1990) 841–850, https://doi.org/10.1127/ejm/2/6/0841.
[66] G. Li, P. Le Bescop, M. Moranville-Regourd, Synthesis of the U phase ($4CaO.0.9Al_2O_3.1.1SO_3.0.5Na_2O.16H_2O$), Cem. Concr. Res. 27 (1997) 7–13, https://doi.org/10.1016/S0008-8846(96)00194-9.
[67] F.P. Glasser, A. Kindness, S.A. Stronach, Stability and solubility relationships in AFm phases: part I. Chloride, sulfate and hydroxide, Cem. Concr. Res. 29 (1999) 861–866, https://doi.org/10.1016/S0008-8846(99)00055-1.
[68] W. Kunther, S. Ferreiro, J. Skibsted, Influence of the Ca/Si ratio on the compressive strength of cementitious calcium–silicate–hydrate binders, J. Mater. Chem. A 5 (2017) 17401–17412, https://doi.org/10.1039/C7TA06104H.
[69] I.G. Richardson, The nature of C-S-H in hardened cements, Cem. Concr. Res. 29 (1999) 1131–1147, https://doi.org/10.1016/S0008-8846(99)00168-4.
[70] F. Avet, E. Boehm-Courjault, K. Scrivener, Investigation of C-A-S-H composition, morphology and density in Limestone Calcined Clay Cement (LC3), Cem. Concr. Res. 115 (2019) 70–79, https://doi.org/10.1016/j.cemconres.2018.10.011.
[71] S.-Y. Hong, F.P. Glasser, Alkali binding in cement pastes: Part I. The C-S-H phase, Cement Concr. Res. 29 (1999) 1893–1903, https://doi.org/10.1016/S0008-8846(99)00187-8.
[72] A. Vollpracht, B. Lothenbach, R. Snellings, J. Haufe, The pore solution of blended cements: a review, Mater. Struct. 49 (2016) 3341–3367, https://doi.org/10.1617/s11527-015-0724-1.
[73] K. Andersson, B. Allard, M. Bengtsson, B. Magnusson, Chemical composition of cement pore solutions, Cem. Concr. Res. 19 (1989) 327–332, https://doi.org/10.1016/0008-8846(89)90022-7.
[74] K.H. Gayer, L. Woontner, The solubility of ferrous hydroxide and ferric hydroxide in acidic and basic media at 25, J. Phys. Chem. 60 (1956) 1569–1571, https://doi.org/10.1021/j150545a021.
[75] D.A. Kulik, Improving the structural consistency of C-S-H solid solution thermodynamic models, Cem. Concr. Res. 41 (2011) 477–495, https://doi.org/10.1016/j.cemconres.2011.01.012.
[76] S. Donatello, A. Fernández-Jimenez, A. Palomo, Very high volume fly ash cements. Early age hydration study using Na 2 SO 4 as an activator, J. Am. Ceram. Soc. 96 (2013) 900–906, https://doi.org/10.1111/jace.12178.
[77] J. Fu, A.M. Jones, M.W. Bligh, C. Holt, L.M. Keyte, F. Moghaddam, S.J. Foster, T. D. Waite, Mechanisms of enhancement in early hydration by sodium sulfate in a slag-cement blend – insights from pore solution chemistry, Cem. Concr. Res. 135 (2020) 106110, https://doi.org/10.1016/j.cemconres.2020.106110.
[78] B.Z. Dilnesa, B. Lothenbach, G. Renaudin, A. Wichser, D.A. Kulik, Synthesis and characterization of hydrogarnet $Ca_3(Al_xFe_{1-x})_2(SiO_4)_y(OH)_{4(3-y)}$, Cem. Concr. Res. 59 (2014) 96–111, https://doi.org/10.1016/j.cemconres.2014.02.001.
[79] B.Z. Dilnesa, E. Wieland, B. Lothenbach, R. Dähn, K.L. Scrivener, Fe-containing phases in hydrated cements, Cem. Concr. Res. 58 (2014) 45–55, https://doi.org/10.1016/j.cemconres.2013.12.012.
[80] F. Georget, V. Caprai, A. Belli, A. Keulen, T. Matschei, Investigation of a supplementary cementitious material with three reactive components: the example of a carbonated mineral composite, Cem. Concr. Compos. 163 (2025) 106–179, https://doi.org/10.1016/j.cemconcomp.2025.106179.
[81] C. Venkatesh, R. Nerella, M.S.R. Chand, Role of red mud as a cementing material in concrete: a comprehensive study on durability behavior, Innov. Infrastruct. Solut. 6 (2021) 13, https://doi.org/10.1007/s41062-020-00371-2.
[82] J. Lee, T. Lee, Durability and engineering performance evaluation of CaO content and ratio of binary blended concrete containing ground granulated blast-furnace slag, Appl. Sci. 10 (2020) 2504, https://doi.org/10.3390/app10072504.
[83] F. Deschner, F. Winnefeld, B. Lothenbach, S. Seufert, P. Schwesig, S. Dittrich, F. Goetz-Neunhoeffer, J. Neubauer, Hydration of Portland cement with high replacement by siliceous fly ash, Cem. Concr. Res. 42 (2012) 1389–1400, https://doi.org/10.1016/j.cemconres.2012.06.009.
[84] S. Song, H.M. Jennings, Pore solution chemistry of alkali-activated ground granulated blast-furnace slag, Cem. Concr. Res. 29 (1999) 159–170, https://doi.org/10.1016/S0008-8846(98)00212-9.
[85] J.-Z. Zhou, G.-R. Qian, Y.-L. Cao, P.-C. Chui, Y.-F. Xu, Q. Liu, Transition of Friedel phase to chromate-AFm phase, Adv. Cem. Res. 20 (2008) 167–173, https://doi.org/10.1680/adcr.2008.20.4.167.
[86] B. Lothenbach, A. Nonat, Calcium silicate hydrates: solid and liquid phase composition, Cem. Concr. Res. 78 (2015) 57–70, https://doi.org/10.1016/j.cemconres.2015.03.019.
[87] B. Mota, T. Matschei, K. Scrivener, The influence of sodium salts and gypsum on alite hydration, Cem. Concr. Res. 75 (2015) 53–65, https://doi.org/10.1016/j.cemconres.2015.04.015.
[88] G. Mertens, R. Snellings, K.V. Balen, B. Bicer-Simsir, P. Verlooy, J. Elsen, Pozzolanic reactions of common natural zeolites with lime and parameters affecting their reactivity, Cem. Concr. Res. 39 (2009) 233–240, https://doi.org/10.1016/j.cemconres.2008.11.008.
[89] F. Zhu, X. Guo, Y. Shi, G. Wang, C. Du, J. Jiang, Y. Wu, W. Hartley, S. Xue, Ecological restoration affects the dynamic response of alkaline minerals dissolution in bauxite residue, Sci. Total Environ. 912 (2024) 169364, https://doi.org/10.1016/j.scitotenv.2023.169364.
[90] T. Radomirovic, P. Smith, D. Southam, S. Tashi, F. Jones, Crystallization of sodalite particles under Bayer-type conditions, Hydrometallurgy 137 (2013) 84–91, https://doi.org/10.1016/j.hydromet.2013.05.006.
[91] G. Engelhardt, J. Felsche, P. Sieger, The hydrosodalite system Na6+ x [SiAlO4] 6 (OH) x. cntdot. nH2O: formation, phase composition, and de-and rehydration studied by 1H, 23Na, and 29Si MAS-NMR spectroscopy in tandem with thermal analysis, x-ray diffraction, and IR spectroscopy, J. Am. Chem. Soc. 114 (1992) 1173–1182, https://doi.org/10.1021/ja00030a008.
[92] M.T. Weller, Where zeolites and oxides merge: semi-condensed tetrahedral frameworks, J. Chem. Soc. Dalton Trans. (2000) 4227–4240, https://doi.org/10.1039/B003800H.
[93] R. Snellings, Solution-controlled dissolution of supplementary cementitious material glasses at pH 13: the effect of solution composition on glass dissolution rates, J. Am. Ceram. Soc. 96 (2013) 2467–2475, https://doi.org/10.1111/jace.12480.
[94] A. Kumar, G. Sant, C. Patapy, C. Gianocca, K.L. Scrivener, The influence of sodium and potassium hydroxide on alite hydration: experiments and simulations, Cem. Concr. Res. 42 (2012) 1513–1523, https://doi.org/10.1016/j.cemconres.2012.07.003.
[95] S.-Y. Hong, F. Glasser, Alkali binding in cement pastes: part I. The CSH phase, Cement Concr. Res. 29 (1999) 1893–1903.
[96] E. L'Hôpital, B. Lothenbach, K. Scrivener, D. Kulik, Alkali uptake in calcium alumina silicate hydrate (CASH), Cem. Concr. Res. 85 (2016) 122–136, https://doi.org/10.1016/j.cemconres.2016.03.009.
[97] D. Wang, Q. Zhang, Y. Feng, Q. Chen, C. Xiao, H. Li, Y. Xiang, C. Qi, Hydration and mechanical properties of blended cement with copper slag pretreated by thermochemical modification, Materials (Basel, Switzerland) 15 (2022) 3477, https://doi.org/10.3390/ma15103477.
[98] J. Siramanont, Effect of Ions and Admixtures on the Growth of Synthetic Calcium Silicate Hydrate (C-S-H). https://infoscience.epfl.ch/handle/20.500.14299/149663, 2018 (accessed January 19, 2026).
[99] D. Hou, W. Zhang, J. Sun, J. Zhang, Structure, dynamics and mechanical properties evolution of calcium-silicate-hydrate induced by Fe ions: a molecular dynamics study, Construct. Build. Mater. 287 (2021) 122875, https://doi.org/10.1016/j.conbuildmat.2021.122875.

[100] N.K. Labhasetwar, O.P. Shrivastava, Y.Y. Medikov, Mössbauer study on iron-exchanged calcium silicate hydrate: $Ca_{5-x}Fe_xSi_6O_{18}H_2 \cdot nH_2O$, J. Solid State Chem. 93 (1991) 82–87, https://doi.org/10.1016/0022-4596(91)90277-O.
[101] A. Mancini, E. Wieland, G. Geng, B. Lothenbach, B. Wehrli, R. Dähn, Fe(II) interaction with cement phases: method development, wet chemical studies and X-ray absorption spectroscopy, J. Colloid Interface Sci. 588 (2021) 692–704, https://doi.org/10.1016/j.jcis.2020.11.085.
[102] Y. Liu, Y. Zhang, L. Li, T.-C. Ling, Impact of limestone–metakaolin ratio on the performance and hydration of ternary blended cement, J. Mater. Civ. Eng. 35 (2023) 04023027, https://doi.org/10.1061/(ASCE)MT.1943-5533.0004685.
[103] J.J. Wolf, D. Jansen, F. Goetz-Neunhoeffer, J. Neubauer, Impact of varying Li2CO3 additions on the hydration of ternary CSA-OPC-anhydrite mixes, Cem. Concr. Res. 131 (2020) 106015, https://doi.org/10.1016/j.cemconres.2020.106015.
[104] B.Z. Dilnesa, B. Lothenbach, G.L. Saout, G. Renaudin, A. Mesbah, Y. Filinchuk, A. Wichser, E. Wieland, Iron in carbonate containing AFm phases, Cem. Concr. Res. 41 (2011) 311–323, https://doi.org/10.1016/j.cemconres.2010.11.017.
[105] B.Z. Dilnesa, B. Lothenbach, G. Renaudin, A. Wichser, E. Wieland, Stability of monosulfate in the presence of iron, J. Am. Ceram. Soc. 95 (2012) 3305–3316, https://doi.org/10.1111/j.1551-2916.2012.05335.x.
[106] A. Lechevallier, Y. Bai, A. Rochelet, R. Thirouard, M. Chaouche, E. Prat, J. Soudier, G. Renaudin, The monocarbonate Ca2Al1-xFex(OH)6·½CO3·nH2O AFm system, Cem. Concr. Res. 190 (2025) 107804, https://doi.org/10.1016/j.cemconres.2025.107804.
[107] W. Kunther, Z. Dai, J. Skibsted, Thermodynamic modeling of hydrated white Portland cement–metakaolin–limestone blends utilizing hydration kinetics from 29Si MAS NMR spectroscopy, Cem. Concr. Res. 86 (2016) 29–41, https://doi.org/10.1016/j.cemconres.2016.04.012.
[108] F. Zunino, K. Scrivener, Assessing the effect of alkanolamine grinding aids in limestone calcined clay cements hydration, Construct. Build. Mater. 266 (2021) 121293, https://doi.org/10.1016/j.conbuildmat.2020.121293.
[109] J. Xu, P. Chen, Synergistic effect of iron tailings, steel slag and red mud cementitious materials on mechanical and microstructure properties, J. Build. Eng. 95 (2024) 110131, https://doi.org/10.1016/j.jobe.2024.110131.
[110] X. Hao, X. Liu, Z. Zhang, W. Zhang, Y. Lu, Y. Wang, T. Yang, In-depth insight into the cementitious synergistic effect of steel slag and red mud on the properties of composite cementitious materials, J. Build. Eng. 52 (2022) 104449.
[111] M. Georgiades, C. Özcan Kilcan, M. Giels, T. Hertel, Y. Pontikes, A.H. Tkaczyk, C. Cheeseman, R.J. Myers, Ex ante life cycle assessment of bauxite residue vitrification technology, Int. J. Life Cycle Assess. 30 (2025) 1896–1911, https://doi.org/10.1007/s11367-025-02512-0.
[112] Z. Yue, X. Zhu, Microstructural insights and technical challenges of effectively adopting high-volume GGBS in blended cements for low-carbon construction, Npj Mater. Sustain. 3 (2025) 25, https://doi.org/10.1038/s44296-025-00070-y.
[113] P.B. Cusack, R. Courtney, M.G. Healy, L.M.T.O. Donoghue, É. Ujaczki, An evaluation of the general composition and critical raw material content of bauxite residue in a storage area over a twelve-year period, J. Clean. Prod. 208 (2019) 393–401, https://doi.org/10.1016/j.jclepro.2018.10.083.
[114] CEN/TC-51 (Technical Committee on Cement) (Ed.), Guidelines for a Procedure to Support the European Standardization of Cements, 2018, https://doi.org/10.31030/2856650.